ELSEVIER

ENGINEERING STRUCTURES

Check for updates

Experimental and numerical studies of tubular concrete structures subjected to blast loading

Martin Kristoffersen [a,b,*], Knut Ove Hauge [c], Arianna Minoretti [d], Tore Børvik [a,b]

[a] Structural Impact Laboratory (SIMLab), Department of Structural Engineering, Norwegian University of Science and Technology (NTNU), Rich. Birkelands vei 1A, NO-7491 Trondheim, Norway
[b] Centre for Advanced Structural Analysis (CASA), NTNU, NO-7491 Trondheim, Norway
[c] Norwegian Defence Estates Agency (NDEA), NO-0103 Oslo, Norway
[d] Norwegian Public Roads Administration (NPRA), Abels gate 5, NO-7030 Trondheim, Norway

ABSTRACT

The E39 coastal highway route along the west coast in Norway is envisioned a future without ferries. A submerged floating tube bridge built in concrete has been suggested as a means of crossing wide and deep fjords, and an internal blast load against this structure could have disastrous consequences. To investigate the response of tubular concrete structures subjected to blast loading, standard off-the-shelf concrete pipes were tested using live explosives. The tests were monitored by high-speed cameras and pressure sensors. Three different positions for the explosive charges were used and the charge size was varied for each position. It was found that a contact charge detonated from the outside requires approximately twice the explosive amount to breach the pipe than a contact charge detonated from the inside, suggesting a significant confinement effect. Charges placed in the centre of the cross-section produced longitudinal cracking and fragmentation. Measurements show that the pressure inside the pipe is notably higher than immediately outside. As one would expect, reinforcement increased the blast capacity of the pipes significantly. Material test specimens (cubes and cylinders) were cut from the pipes and tested quasi-statically to determine the mechanical properties. The material tests were used to calibrate a concrete material model for finite element simulations, where the blast load was described by a particle-based method. The structural response from the simulations showed good agreement with the experimental data. This applied to the contact charges as well although no special measures were taken to account for the contact detonation.

1. Introduction

The E39 Coastal Highway Route project [1] aims to replace all the ferries along the E39 route on the west coast of Norway with fixed connections. Some of the fjord crossings are too wide and deep for conventional strait crossing structures like suspension bridges or underwater rock tunnels. One of the proposed solutions to crossing these fjords is a submerged floting tube bridge (SFTB) in concrete [2]. This type of structure was proven to be feasible for crossing the Høgsfjord in Norway, acting as a basis for furhter development of the SFTB [3]. An SFTB has been suggested for locations all over the world: Funka bay, Japan [4,5], Messina strait, Italy [6,7], Qiandao lake, China [8,9], and Bjørnafjord, Norway [10]. While such a structure has not been built yet,

it has been analysed for various loading scenarios, e.g. hydrodynamic and/or seismic loads [6,7,9–11], impact loads [12], vehicle loads [13], fluid–structure interaction [14,15], and cable failure [16]. Blast loading caused either by a terrorist attack or by an accident involving tankers carrying flammable goods could have disastrous consequences for an SFTB. This kind of load case has so far only been investigated numerically [17–19]. Full-scale testing of a blast load scenario in an SFTB is not a feasible option, thus physical testing has to be carried out on smaller samples which still capture the main physics of blast loading in tubular concrete structures.

Concrete structures exposed to blast loading has been extensively studied through several approaches – experimentally [20,21], numerically [22,23], analytically/empirically [24,25], or any combination of
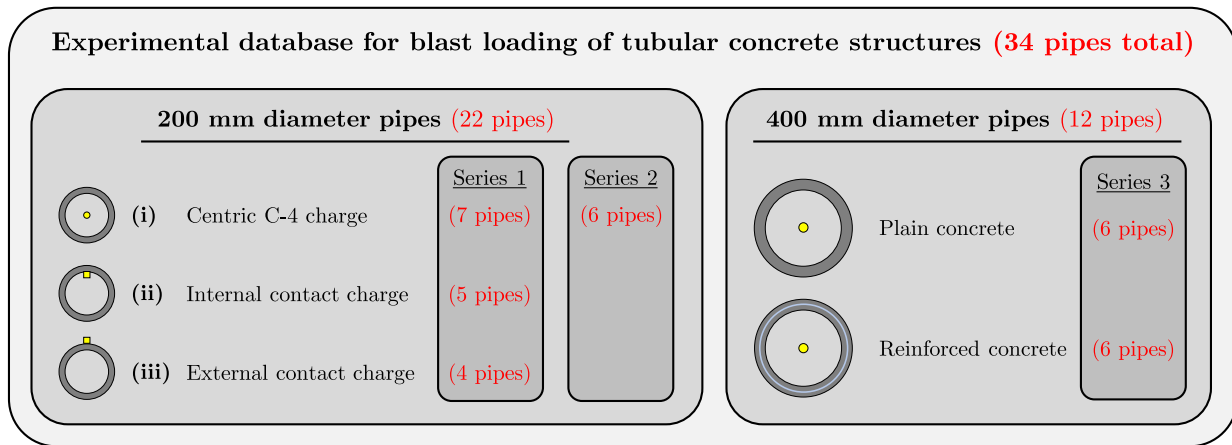

Fig. 1. Overview of experimental database presented in this study.

these [26–30]. A recent study by Yang et al. [31] utilised experiments for validation of numerical models which were later used to simulate blast loads against an underwater tunnel in concrete and to evaluate protective measures. Dam structures subjected to close-in underwater blast loading have been examined numerically by Zhao et al. [32], who found that detonations inside the dam openings cause far greater damage than detonations outside. The same conclusion was reached by Pan et al. [33] by simulating detonations at various positions on a bridge deck cross-section. Colombo et al. [34] used a shock tube to study the performance of a protective layer intended for internal use in tunnels through soil. While fibre reinforcement is not part of this study, it has been found to have mitigating effects on blast loading against concrete [35,36], and can improve the post-blast static behaviour [37]. Other blast mitigation tactics may also be applicable to concrete structures like SFTBs [20,29,38–40].

This work investigates the behaviour of tubular concrete structures subjected to blast loading. The first goal was to build an elaborate experimental database of the structural behaviour and pressure measurements, both of which can be used for validation of numerical models. This study will concentrate on the structural behaviour while a detailed analysis of the pressure data is left for further work. Still, the most important results are included here. To the authors' knowledge, there is no experimental data in the open literature on blast loading of tubular concrete structures. Here, two different internal pipe diameters were used, 200 mm and 400 mm as shown later in Fig. 4. 22 of the former and 12 of the latter have been used to produce a rich experimental database. An overview can be seen in Fig. 1, where different charge positions and the effect of reinforcement were the most important test parameters. In addition, material test specimens were extracted from the pipes and tested quasi-statically. Note that the pipes are not to be considered as small-scale versions of an SFTB, but as generic tubular concrete structures.

The second goal was to investigate whether finite element simulations were able to reproduce some key experimental results. The goal is not to achieve a 1-to-1 correspondence between tests and simulations, but to determine the capabilities of the chosen approach in terms of structural response and to highlight some important features. A proper comparison of the blast load and its distribution is out of scope for the current work. In general, the FE simulations were able to capture the main trends observed in the test programme.

2. Material testing

2.1. Concrete

The concrete had a water to cement ratio of 0.37 and the aggregate size was 0–8 mm, which means that the diameter (or cube length) of test specimens should be at least 28 mm [41]. 10 cylindrical samples with nominal diameter 32 mm and height 40 mm (height to diameter ratio = 1.25) were thus cored from the 200 mm pipes, and 5 cubes with sides 40 mm were cut from the pipe wall. Both pipe geometries were made from the same concrete recipe. The specimens were used for compression tests and tensile splitting tests performed in an Instron 5985 250 kN universal testing machine at a deformation rate of 0.24 mm/min (initial strain rate of 10^{-4} s^{-1} for the cylinder and cube compression tests). The surfaces were ground plane and parallel to prevent skewed loading. For the tensile splitting tests, wooden strips were used to create a line load along each cylindrical specimen's main axis. All test specimens were painted with a speckled pattern for use with digital image correlation (DIC) [42], which has been shown to work for both small [43] and large [44] deformations. The DIC data was later used for calibration of a concrete model.

The force–displacement curves from the tests are shown in Fig. 2. The specimens were labelled 1–15; the cube tests 1–5 (a), the cylinder
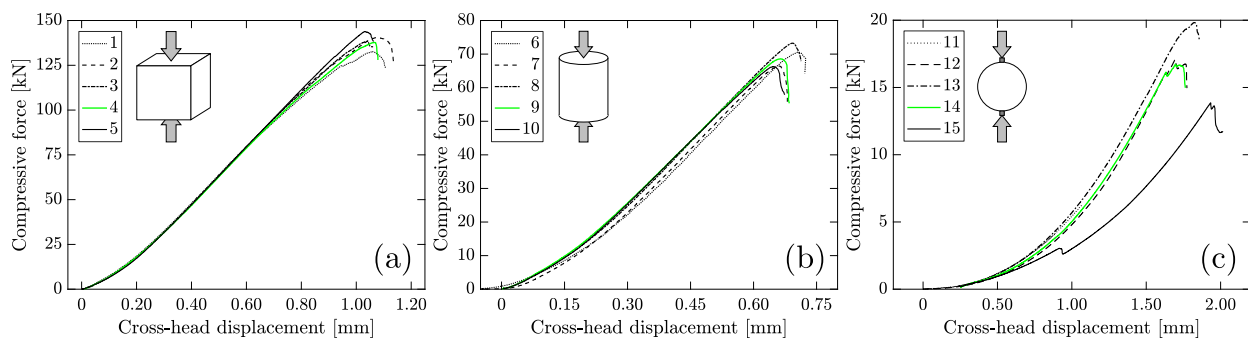

Fig. 2. Force–displacement curves from (a) cube compression test, (b) cylinder compression tests, and (c) tensile splitting tests as logged from the test rig.
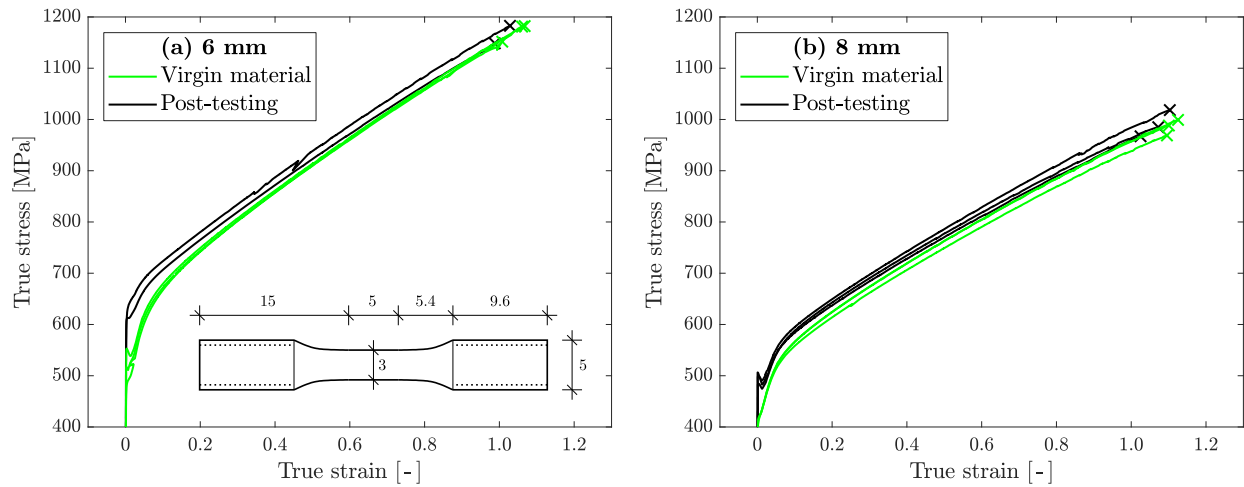
Fig. 3. True stress-true strain curves from quasi-static tension tests for (a) the 6 mm bars in the hoop direction, and (b) the 8 mm bars in the longitudinal direction.

Table 1
Results from quasi-static tension tests of reinforcement bars.

Condition	Direction	Diameter	σ_0 [MPa]	S_{UTS} [MPa]	e_{UTS} [–]	σ_{max} [MPa]	ε_{frac} [–]
virgin	hoop	6 mm	517.3	612.9	0.159	1169.8	1.045
post-test	hoop	6 mm	619.8	684.4	0.081	1163.6	1.003
virgin	longitudinal	8 mm	417.1	511.6	0.146	985.0	1.107
post-test	longitudinal	8 mm	494.5	533.1	0.120	990.5	1.067

compression tests 6–10 (b), and the tensile splitting tests 11–15 (c). Both the cube and cylinder compression tests were quite consistent, while the tensile splitting (Brazilian) tests were more scattered. During testing of specimen 11, a data transfer error occured and the data for this test is therefore incomplete as shown in Fig. 2(c). Specimen 15 had a sudden drop in the force, the cause of which was difficult to determine from the images. The data from test 15 was thus discarded. The shape of all the curves in Fig. 2 is curved in the beginning, and then becomes linear. This is because each surface of each specimen is not 100% parallel and flat, meaning that contact with the rig is not initiated simultaneously across the entire surface. In the tensile splitting tests, this is more pronounced due to the wooden strips placed along the axis of the cylindrical specimens. This also resulted in a larger cross-head displacement which is not representative for the cylinder behaviour, thereby warranting local measurements like DIC.

The 28 day cube compressive strength tests performed by the concrete pipe factory gave a value of 83.3 MPa. Based on Fig. 2(a), the average cube compressive strength was 86.3 MPa. The mean value from the cylinder tests was 81.8 MPa. A correction factor of 0.93 for a ratio of 1.25 is given in ASTM C42/C42M [45], resulting in an estimated cylinder (uniaxial) compressive strength of $f_c = 76.1$ MPa. The average tensile strength was estimated to $f_t = 3.2$ MPa [46], and the mass density was measured to 2440 kg/m^3.

2.2. Steel reinforcement

6 out of 12 of the 400 mm diameter concrete pipes were reinforced (see Fig. 1). Two different reinforcement diameters were used for each pipe, 6 mm for the hoop direction and 8 mm for the longitudinal direction. Axisymmetric specimens with geometry as shown in Fig. 3(a) were machined from both reinforcement diameters. The hoop reinforcement was dodecagon-shaped, making specimen extraction easy. The virgin material of the reinforcement bars was tested along with samples extracted from a pipe post-testing (test R400-XI) for comparison. A general purpose displacement controlled Zwick testing machine operating at a deformation rate of 0.3 mm/min was used for the quasi-

static testing (initial strain rate of $\dot{\varepsilon}_0 = 10^{-3}$ s^{-1}). The force, the cross-head displacement and the specimen's diameter reduction in two perpendicular directions were continuously measured all the way to fracture [47], thus providing valid data beyond the point of necking.

The quasi-static tensile test results are plotted as true stress-true strain curves in Fig. 3, where (a) contains results for the 6 mm circumferential bars and (b) for the 8 mm longitudinal bars. It is noted that the stress–strain values in Fig. 3 are average values across the minimum cross-section of the specimen. Table 1 lists the main test results, which are the yield stress σ_0, the ultimate tensile stress S_{UTS}, the engineering strain at the ultimate tensile stress e_{UTS}, the maximum true stress σ_{max}, and finally the true fracture strain $\varepsilon_{frac} = 2\ln(D_0/D_f)$ where D_0 is the initial diameter and D_f is diameter at fracture measured by a micrometer. The values given in Table 1 are average values from three tests of each configuration. Generally, the stress parameters σ_0, S_{UTS}, and σ_{max} are notably higher for the 6 mm circumferential bars compared with the 8 mm longitudinal bars.

From both Table 1 and Fig. 3 it is clear that the reinforcement has undergone plastic deformations in the blast test, evident through the increased yield stress. The effect of the blast test on the true stress-true strain curves diminishes with increasing plastic strain. The ductility as measured by ε_{frac} is similar across all material tests, but decreases along with e_{UTS} for the post-test specimens. Because none of the reinforcement bars failed in any of the blast tests, this is not of great importance. The ratio of the diameter reductions in two perpendicular directions was close to unity for all tests, indicating an isotropic material. In addition, the fracture surfaces were circular.

3. Component testing

3.1. Description of concrete pipes

The concrete pipes used herein are standard off-the-shelf concrete pipes intended for drainage. The advantage of using mass produced specimens is consistency – the material and geometrical properties are very similar from one specimen to the next. Two different pipe geome-
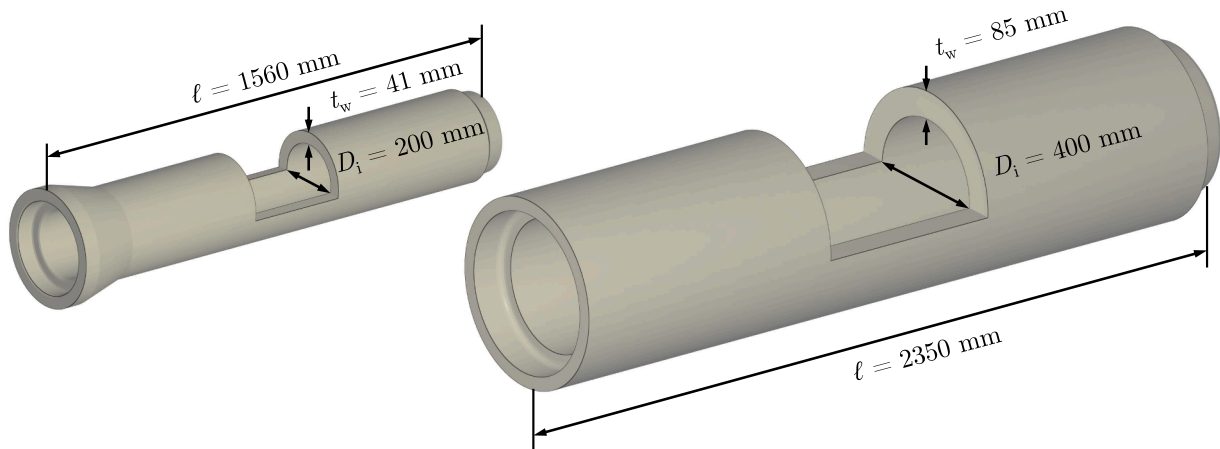
Fig. 4. Geometry of concrete pipes P200 (left) and P400/R400 (right) used for blast load experiments in this study.

tries were used, $D_i = 200$ mm and $D_i = 400$ mm as shown in Fig. 4, where the pipe wall thickness t_w and the total pipe length ℓ are given as well. The smaller of the two pipes was always plain concrete (called P200), while the larger was either plain (P400) or reinforced concrete (R400). The longitudinal reinforcement for the R400 pipes was 12 bars of diameter 8 mm, equally distributed across the cross-section. A dodecagon helix with 100 mm loop spacing along the pipe made up the hoop reinforcement, and was placed on the outside of and spot welded to the longitudinal bars. The reinforcement layer was placed in the middle of the pipe wall thickness, making the diameter of the helix approximately 485 mm. The pipes have flanges at each end to enable connecting them to form a long continuous drainage pipe.

3.2. Setup of blast tests

Three main series of blast tests have been conducted as outlined in Fig. 1, where the overarching goal of the three series was to investigate the behaviour of tubular concrete structures subjected to blast loading. In all series, the pipes were placed on wooden planks for support, and wedges were used to prohibit rolling. Pressure sensors were used to monitor the blast wave propagation and magnitude, and were in most cases mounted to 400 mm × 400 mm × 30 mm aluminium plates. The top of the aluminium plates were adjusted to be level with the bottom of the inside of the pipe in all cases. All tests were filmed from two angles with high-speed cameras. The blast was generated by a plastic explosive charge (composition C-4) of various sizes. An electrically ignited blasting cap (equivalent to approximately 1 g of C-4) was used to initiate the blast for all tests herein.

The first series investigated the effect of charge placement on the response of P200 pipes, and determined the charge size needed to breach the pipe from three different positions: (i) centrically placed in the cross-section, (ii) in contact with the pipe wall on the inside, and (iii)

in contact with the pipe wall on the outside. The second test series repeated the position (i) tests with more pressure sensors, including two sensors mounted on the P200 pipe itself. This enabled monitoring of the pressure inside the pipe as well so the pressure inside and immediately outside could be compared. The third and final series used the same test setup as in the second series, but was now used to investigate the difference in response between reinforced (R400) and plain (P400) concrete pipes with larger diameters. All tests will also serve as possible validation cases for numerical simulations (presented later). Only charge position (i) was used for the latter two series. For position (i) the Hopkinson-Cranz scaled distance Z is

$$Z = \frac{R}{\sqrt[3]{W}} \tag{1}$$

in which R is the distance from the centre of the charge to the target, and W is the charge weight. Similar Z-values should give similar pressure–time response (assuming a free air blast). For the contact charges in series 1, this measure does not make sense because $R = 0$. The range of validity of Eq. (1) is for $Z > 0.16$ m/kg$^{1/3}$ [48]. The following three sections will describe the test setup and results of each series.

4. Series 1 – P200 charge placement

4.1. Setup of series 1

The setup for this series is illustrated in Fig. 5. Parts of this test series were presented in [49], and is included here for completeness. For charge position (i) the charge was spherical and was placed on a styrofoam support. In case (ii) the charge was shaped like a cube, and was held against the pipe wall using a thin styrofoam spring. In the final case (iii), the cubic charge was held in contact with the pipe wall by tightening the detonation cord slightly. A charge size of 10.0 g was used for
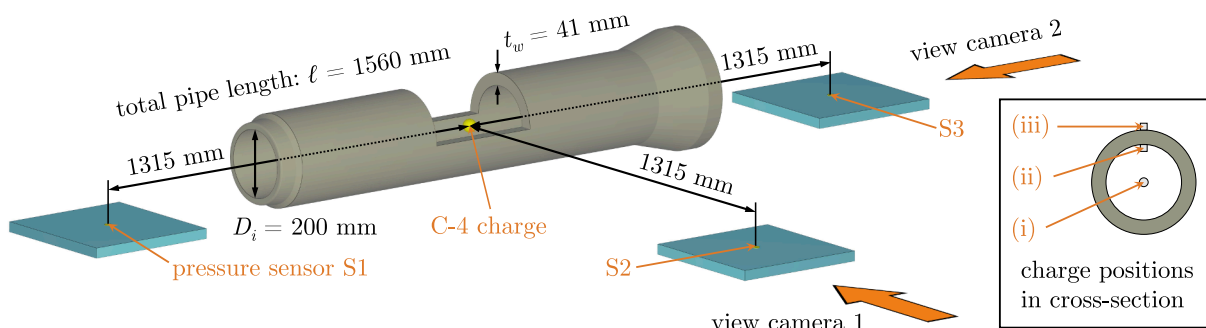

Fig. 5. Setup of test series 1 including the different charge positions, (i) centrically in the cross-section, (ii) contact inside, and (iii) contact outside.

Table 2
Complete experimental matrix for test series 1 sorted by charge position and charge size.

ID	position	R	W	Z	P_1	P_2	P_3	comment
		[mm]	[g]	[m/kg$^{1/3}$]	[kPa]	[kPa]	[kPa]	(crater/hole sizes in [cm])
P200-III	(i)	100	10.0	0.464	168	21	222	Pipe remained intact
P200-IV	(i)	100	12.5	0.431	213	24	264	Longitudinal surface cracks
P200-XIV	(i)	100	13.0	0.425	200	31	240	Few and large oblong pieces
P200-VI	(i)	100	13.5	0.420	210	17	269	Few and large oblong pieces
P200-V	(i)	100	14.0	0.415	203	29	257	Few and large oblong pieces
P200-II	(i)	100	15.0	0.405	227	25	277	Few and medium oblong pieces
P200-I	(i)	100	25.0	0.342	332	28	321	Many medium/small oblong pieces
P200-VIII	(ii)	-	5.0	-	119	16	143	Crater 13 × 13
P200-XV	(ii)	-	6.0	-	123	28	149	Crater 15 × 13, hole 2 × 2
P200-IX	(ii)	-	7.5	-	131	28	171	Crater 14 × 16, hole 2 × 2
P200-X	(ii)	-	7.5	-	152	86	183	Crater 14 × 16, hole 2 × 2
P200-VII	(ii)	-	10.0	-	139	18	202	Few oblong pieces + crater
P200-XI	(iii)	-	10.0	-	34	45	33	Crater 7 × 9
P200-XVI	(iii)	-	12.5	-	47	114	89	Crater 9 × 11, hole 1 × 2
P200-XII	(iii)	-	15.0	-	28	81	57	Crater 8 × 11, hole 3 × 3
P200-XIII	(iii)	-	20.0	-	72	125	91	Crater 11 × 13, hole 4 × 5

Fig. 6. Fragmented P200 pipes after testing with spherical C-4 charges detonated from position (i), for (a) 13.0 g, (b) 15.0 g, and (c) 25.0 g.

all three charge positions to observe possible differences in response due to charge placement alone. While the charge shape may exert some influence on the load and hence the response of the structure [50–52], this subject is considered out of scope for the current work.

To monitor the pressure, three Kistler 603B pressure sensors (sampling rate of 1 MHz) were placed at equidistant positions 1315 mm from the charge as shown in Fig. 5. Two Phantom v2012 high speed cameras inside protective containers recording at 22 600 fps captured the experiments from two angles (resolution 1 280 × 800 pixels). The ambient temperature during testing was approximately 8–10 °C. The complete experimental matrix for test series 1 is listed in Table 2, where P_1 to P_3 are the maximum pressures recorded by sensors S1 to S3, respectively. The pipes are identified by a roman numeral following the chronological order in which the tests were conducted.

4.2. Test results of series 1

The experimental campaign started out by detonating charges from position (i), from which a charge size of 13.0 g (pipe P200-XIV) was needed to breach the pipe. Decreasing the charge size to 12.5 g produced only longitudinal surface cracks. The smallest charge size in position (i), 10.0 g for pipe P200-III, caused no visible damage to the pipe. For the

higher charge sizes (13.0 g and above), the pipe suffered longitudinal through-thickness cracks before pieces fragmented from the pipe. Increasing the charge size generally produced smaller and more fragments, as illustrated in Fig. 6. Longitudinal cracks were expected, because the pressure in the hoop direction of a closed cylindrical pressure vessel is about twice the pressure in the longitudinal direction [53]. Additionally, there are no end caps on the pipes to retain the pressure in the longitudinal direction. The brittle behaviour with longitudinal cracks and oblong pieces is radically different from ductile materials like steel, where the steel typically bulges severely due to radial expansion before rupturing [52,54,55]. The images in Fig. 7 from the high-speed video of pipe P200-XIV (13.0 g C-4) illustrate the typical behaviour of fragmenting concrete pipes with (a) longitudinal cracking, (b) fragments forming, and (c) pieces detaching from the pipe.

Moving on to charge position (ii), the amount of explosive needed to breach the pipe was approximately halved to 6.0 g. In addition to producing the longitudinal cracks as seen for the previous case, a burst of concrete debris rose up from the location of the charge. Local scabbing and spalling damage was produced on both sides of the pipe for all charge sizes. For the 5.0 g charge, scabbing and spalling was the only visible damage (see Fig. 8(a)). The damage progressing from 5.0 g to 7.5 g is shown in Fig. 8, from only surface damage in (a), to through-
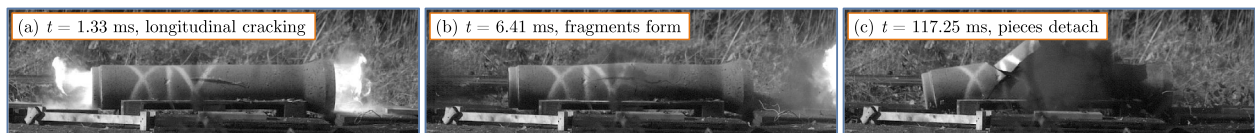
Fig. 7. Images from high-speed footage of pipe P200-XIV at (a) 1.33 ms, (b) 6.41 ms and (c) 117.25 ms after detonating a 13.0 g C-4 charge at position (i).

Fig. 8. Damage to P200 pipes after testing with cubic C-4 charges from position (ii), for (a) 5.0 g, (b) 6.0 g, and (c) 7.5 g.
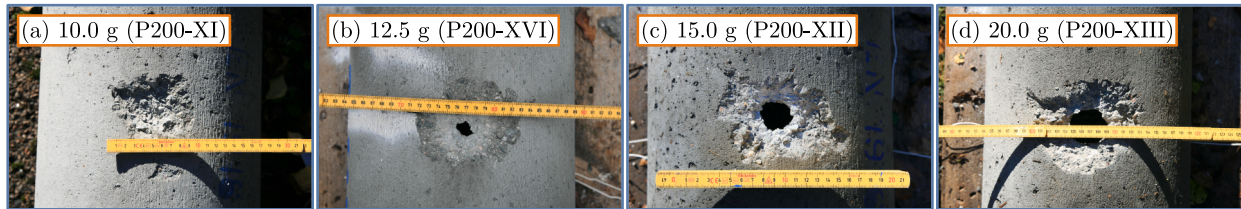

Fig. 9. Damage to P200 pipes after testing with cubic C-4 charges from position (iii), for (a) 10.0 g, (b) 12.5 g, (c) 15.0 g, and (d) 20.0 g.
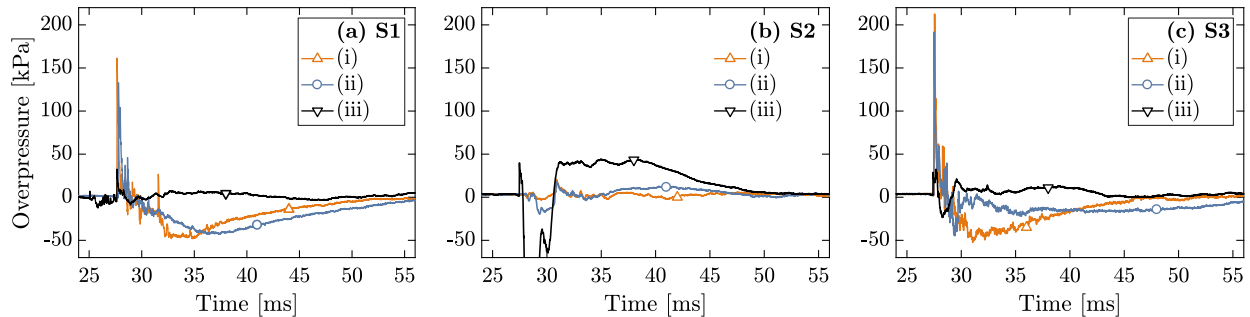

Fig. 10. Pressure–time histories from tests using charge size 10.0 g at positions (i), (ii) and (iii), where part (a) shows data from sensor S1, (b) from sensor S2, and (c) from sensor S3.

thickness cracking with pieces detaching in (b), and finally to full fragmentation in (c). The pieces breaking off were of a somewhat higher aspect ratio compared with the pieces forming from detonations in charge position (i).

For the external contact charges, fragmentation was never observed for the charge sizes used herein (10.0 g to 20.0 g). The 10.0 g charge produced a crater on both sides of the pipe wall, and the smallest charge able to make a hole through the pipe was 12.5 g (shown in Fig. 9(a) and (b), respectively). This result illustrates the confining effect of detonating the charge on the inside, from which approximately half the charge size was needed to breach the pipe. This figure might change with the presence of water outside the pipe. Fig. 9(c) and (d) also show that increasing the charge size beyond 12.5 g simply produces larger holes. Further increase of the charge size would undoubtedly result in even larger holes and eventually fragmentation.

Using the overlapping 10.0 g charge size as reference, the responses of the concrete pipes were quite distinct. For position (i) the pipe remained intact and a fireball was clearly seen exiting the pipe. For position (iii) a small crater was noted on both sides of the pipe wall. In position (ii), the 10.0 g C-4 charge caused significantly more damage to the pipe. A jet of debris was punched out directly above the charge and the pipe suffered longitudinal cracks and fragmentation. In general, internal detonations produced more severe damage as also noted by e.g. Pan et al. [33]. It is worth mentioning that the mouths of each pipe remained intact in all the tests, indicating that blast loading will primarily be a local load for an SFTB.

Results from the pressure measurements will for brevity be limited to the difference between positions (i), (ii) and (iii) for the 10.0 g charge. The pressure–time histories from these tests have been plotted in Fig. 10 for all three charge positions, and all three pressure sensors equidistant from the charge as sketched in Fig. 5. Position (i) produced the maximum and minimum extremes of the pressure magnitude, while position (ii) had the longest duration for the negative phase. The pressure data for position (iii) was lower in magnitude and quite different qualitatively. This is because the concrete pipe itself shadows sensors S1 and S3, and there is no confinement effect from this position. Generally the pressure recordings were consistent across the entire test series, with larger charges giving higher pressures (see Table 2). Sensors S1 and S3 gave decent and reliable data, but this has been omitted for brevity (the pressure profiles are discussed in Section 5). The pressure data from sensor S2 was difficult to assess so this particular sensor location was not used in the two subsequent test series. Also, the heat from the fireball appear to influence the negative phase of the pressure recordings somewhat, so the sensors were replaced for the next series. The information gathered from the sensors in series 1 was somewhat limited, and the most interesting area to measure the pressure is inside the pipes. For these reasons, and to keep redundancy in case of sensor failure during a test, the number of sensors was increased for the subsequent tests.
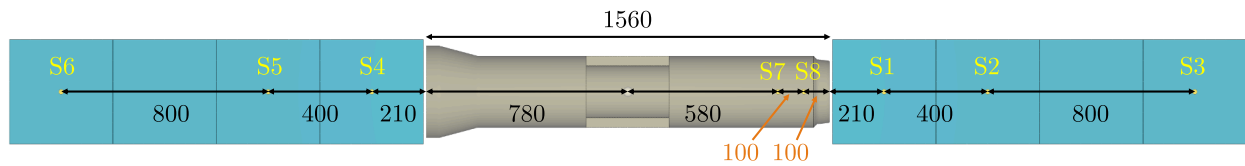
Fig. 11. Sketch of setup of test series 2 (seen from above, measures in mm).

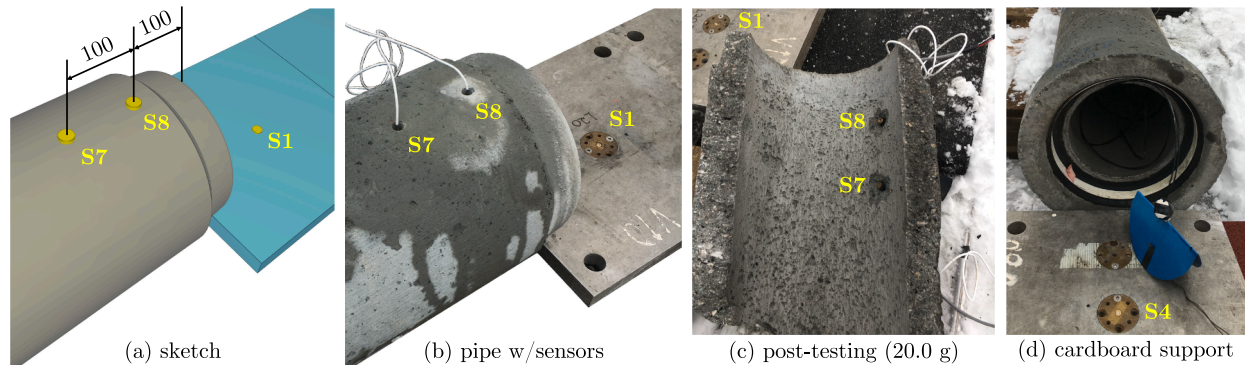| (a) sketch | (b) pipe w/sensors | (c) post-testing (20.0 g) | (d) cardboard support |

Fig. 12. Position of pressure sensors 1, 7 and 8 shown as (a) sketch, (b) mounted in the pipe before testing, and (c) after testing pipe P200-XVII (20.0 g C-4), while (d) shows the cardboard support for the charge.

Table 3
Complete experimental matrix for test series 2 sorted by charge size.

parameter	unit	P200-XVIII		P200-XIX		P200-XX		P200-XXI		P200-XXII		P200-XVII	
R	[mm]	100		100		100		100		100		100	
W	[g]	10.0		12.0		14.0		16.0		18.0		20.0	
Z	[m/kg$^{1/3}$]	0.464		0.437		0.415		0.397		0.382		0.368	
P_1/P_4	[kPa]	640	578	803	487	1106	843	967	825	1009	583	1023*	520
P_2/P_5	[kPa]	–	136	147	54	309	150	–	158	–	189	–	228
P_3/P_6	[kPa]	36	31	40	30	42	36	40	37	38	50	55	55
P_7	[kPa]	1053		1560		4005		1411		2067		1897	
P_8	[kPa]	1317		1695		2143		2076		1897		1721	
t_1/t_4	[ms]	0.80	0.86	0.87	0.86	0.74	0.83	0.73	0.79	0.74	0.72	0.70	0.68
t_2/t_5	[ms]	–	1.52	1.52	1.51	1.30	1.43	–	1.40	–	1.28	–	1.21
t_3/t_6	[ms]	3.40	3.44	3.47	3.44	3.11	3.37	3.11	3.28	3.06	3.13	2.98	2.99
t_7	[ms]	0.41		0.42		0.37		0.35		0.35		0.35	
t_8	[ms]	0.49		0.51		0.44		0.43		0.42		0.41	
i_1^+/i_4^+	[kPa·ms]	79	79	83	78	112	199	110	103	116	57	116	46
i_2^+/i_5^+	[kPa·ms]	–	46	33	30	53	50	–	52	–	57	–	61
i_3^+/i_6^+	[kPa·ms]	23	16	22	14	25	16	22	17	25	14	23	24
i_7^+	[kPa·ms]	489		486		598		598		–		684	
i_8^+	[kPa·ms]	419		394		584		570		613		546	
t_1^+/t_4^+	[ms]	0.50	0.55	0.55	1.36	0.45	2.02	0.41	0.59	0.43	0.23	0.41	0.24
t_2^+/t_5^+	[ms]	–	1.90	1.08	2.03	1.14	1.97	–	1.87	–	1.59	–	1.59
t_3^+/t_6^+	[ms]	1.34	1.33	1.34	1.25	1.60	1.19	1.37	1.38	1.47	1.07	1.43	1.61
t_7^+	[ms]	2.33		2.21		2.25		2.15		–		2.22	
t_8^+	[ms]	2.26		2.28		2.32		2.14		2.17		1.85	
v_{07}	[m/s]	1415		1381		1568		1657		1657		1657	
v_{08}	[m/s]	1388		1333		1545		1581		1619		1659	
v_{78}	[m/s]	1250		1111		1429		1250		1429		1667	
v_{12}/v_{45}	[m/s]	–	606	615	615	714	667	–	656	–	714	–	755
v_{23}/v_{56}	[m/s]	–	417	410	415	442	412	–	426	–	432	–	449

*The sensor recording range was saturated, which means that the peak pressure was higher than this number.
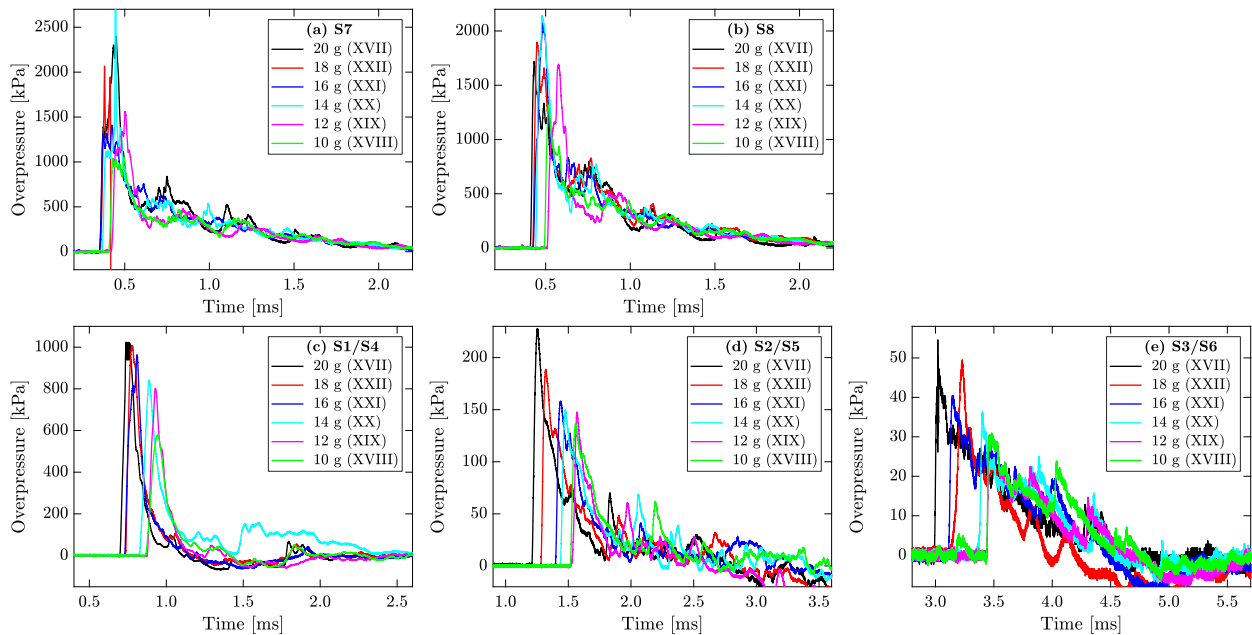
Fig. 13. Pressure recordings from test series 2 from (a) S7, (b) S8, (c) S1/S4, (d) S2/S5 and (e) S3/S6.

5. Series 2 – P200 repeated

5.1. Setup of series 2

The setup for the second test series was based on series 1, which primarily means adding a total of four pressure sensors along the main axis of the pipe (two on each side), and removing what was sensor S2 from the first series. In addition, two sensors were mounted on the pipes directly, resulting in eight sensors in total. A sketch of the setup is shown in Fig. 11, where the labels S1 to S8 indicate Kulite XT-190 pressure sensors (sampling rate 10 MHz). Sensors S7 and S8 were drilled into the pipe 100 mm from the mouth, and with 100 mm distance between them as sketched in Fig. 12(a). Small pieces of the concrete detached from the inside of the pipes because of the drilling, which could potentially weaken the pipe and affect the fragmentation (see Fig. 12(b) and (c)). This might also affect the pressure recordings to some extent.

The C-4 charge is placed in the middle along the pipe's main axis, making S1 and S4 equidistant from the charge (the same applies sensor pairs S2/S5 and S3/S6). Ideally, the pressure data acquired from S1 should therefore be identical to the data from S4 and so on. Having two sensors at equivalent positions gives a backup in case one of them fails, which may happen in blast experiments. In addition, a trigger was added to keep the recordings synchronised and to enable measurement of the arrival times of the shock wave.

Whereas the previous series aimed to determine the minimum charge breaching the P200 pipe, the charge sizes for the current series were predetermined to 10.0 g, 12.0 g, 14.0 g, 16.0 g, 18.0 g and 20.0 g. Based on series 1, 10.0 g and 12.0 g should not breach the pipe, while the remaining four charge sizes should. The charges were always spherical and in position (i) in this test series, and rather than using a Styrofoam support to keep the charge in the centre of the cross-section, a thin cardboard sheet (see Fig. 12(d)) was used to minimise potential effects caused by the support since the cardboard simply burns away.

Like before, two high-speed cameras were used to film the tests from two angles. Due to ongoing work at the test site, the experiments were conducted on a different location where the protective containers for the high-speed cameras were not available. For this reason, somewhat cheaper cameras (Phantom Miro LC310) were used, thus lowering the frame rate to 3 200 fps at 1280 × 800 pixels resolution. This was sufficient to get good images of the events during testing. The test series is summarised in Table 3, where P_1 to P_8 are the peak pressures as registered by each pressure sensor, t_1 to t_8 indicate the time of arrival at each pressure sensor, v_{12} is the estimated shock wave velocity from sensor S1 to sensor S2, and v_{07} from the charge to S7 and so on. Even though the sampling rate was 10 MHz, the time of arrival was rounded off to the nearest hundredth of millisecond. Measuring the distance between the sensors is the larger margin of error anyway. Further, the duration of the positive phase as measured by sensor 1 to 8 is dubbed t_1^+ to t_8^+, and the impulse during this time is denoted i_1^+ to i_8^+. The ambient temperature during testing was approximately 5–8 °C.

5.2. Test results of series 2

The structural behaviour of the pipes was in accordance with expectations. The two smallest charges did not breach the pipe, while the remaining four did. These pipes were from a different batch but the results were still consistent. The material tests in Section 2 were taken from this batch. Increasing the charge size increased the number of fragments and decreased the fragment size, indicating great repeatability from series 1. Some longitudinal surface cracks were noted for the 12.0 g charge. A few cracks were noted in pipe P200-XVII (20.0 g) prior to testing, and this might be the reason why the end flange on one side of pipe broke into pieces (see Fig. 12(c)). This did not happen for any of the pipes in series 1, and it was first thought that the holes for sensors S7 and S8 caused this. However, none of the pipes in this test series had cracks passing through the sensor holes, thereby indicating that the holes did not affect the results to any significant extent.

Fig. 13 shows the pressure–time histories from all six tests in series 2. In part (c) to (e), only the best recording from each sensor pair are shown because a few recordings were atypical or there were some sensor failures. On the whole the data sets are good, and the curve profiles are characteristic for blast loading. In general, the pressure recordings were consistent relative to each other with larger charges producing higher peak pressures. Larger charges also decreased the times of arrival and increased the shock wave velocity. A notable result is that once the shock wave exits the pipe, the pressure is approximately halved as seen in Fig. 13 (note the different ordinate scales). This result means that for confined blast loading, pressure measurements should be conducted inside the confined area to estimate the actual load. Potential clearing effects when the pressure wave exits the pipe and transfers to the
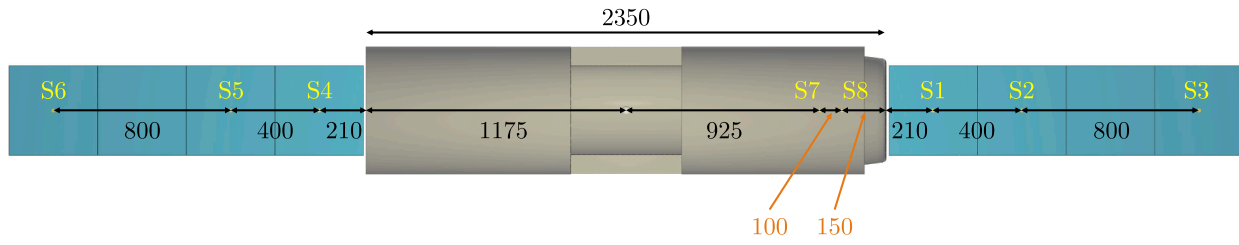
Fig. 14. Sketch of setup of test series 3 (seen from above).

Table 4
Experimental matrix and results for plain concrete pipes in series 3 sorted by charge size.

parameter	unit	P400-VI		P400-X		P400-VII		P400-VIII		P400-V		P400-I	
R	[mm]	200		200		200		200		200		200	
W	[g]	50		65		75		75		100		150	
Z	[m/kg$^{1/3}$]	0.543		0.497		0.474		0.474		0.431		0.376	
P_1/P_4	[kPa]	950	628	941	646	798	663	851	690	989	930	1295	1315
P_2/P_5	[kPa]	417	353	475	429	–	445	–	404	–	638	–	814
P_3/P_6	[kPa]	90	92	107	105	128	113	113	95	164	153	209	205
P_7	[kPa]	782		305		816		569		976		–	
P_8	[kPa]	1117		1298		1199		1172		1656		1782	
t_1/t_4	[ms]	1.17	1.23	1.07	1.12	1.02	1.07	1.06	1.07	0.93	0.95	1.05	0.94
t_2/t_5	[ms]	1.66	1.75	1.54	1.64	1.49	1.58	1.53	1.57	1.33	1.39	1.44	1.32
t_3/t_6	[ms]	3.20	3.32	2.99	3.14	2.86	3.03	2.93	3.06	2.59	2.70	2.59	2.43
t_7	[ms]	0.64		0.59		0.59		0.60		0.52		–	
t_8	[ms]	0.73		0.69		0.68		0.69		0.60		0.75	
i_1^+/i_4^+	[kPa·ms]	212	179	235	194	230	202	235	188	270	264	346	329
i_2^+/i_5^+	[kPa·ms]	138	128	157	136	–	150	–	135	–	178	–	216
i_3^+/i_6^+	[kPa·ms]	77	70	87	69	97	81	82	75	107	102	116	129
i_7^+	[kPa·ms]	108		42		152		113		157		–	
i_8^+	[kPa·ms]	668		681		726		627		914		959	
t_1^+/t_4^+	[ms]	1.13	1.02	1.18	1.04	1.07	1.02	1.10	1.03	1.13	1.04	1.19	0.77
t_2^+/t_5^+	[ms]	1.92	1.82	2.04	2.37	–	2.24	–	2.52	–	2.23	–	1.71
t_3^+/t_6^+	[ms]	3.19	3.34	3.25	3.28	3.63	3.56	2.77	3.81	2.96	3.08	1.20	2.65
t_7^+	[ms]	0.38		0.33		0.35		0.37		0.34		–	
t_8^+	[ms]	3.48		3.23		3.35		3.35		3.32		2.88	
v_{07}	[m/s]	1445		1568		1568		1542		1779		–	
v_{08}	[m/s]	1404		1486		1507		1486		1708		1367	
v_{78}	[m/s]	1111		1000		1111		1111		1250		–	
v_{12}/v_{45}	[m/s]	816	769	851	769	851	784	851	800	1000	909	1026	1053
v_{23}/v_{56}	[m/s]	519	510	552	533	584	552	571	537	635	611	696	721

aluminium plate could also influence the pressure–time histories [56]. Note that in Fig. 13(c), the readings for the 20.0 g charge saturated due to a too low setting for the pressure sensor, and the actual pressure is slightly higher. Local geometrical effects near the sensors like shown in Fig. 12(c) might affect the results, so to obtain optimal pressure readings for a confined space like here the surfaces should be smooth and the sensors properly flush mounted. For this reason, the results from the internal pressure sensors should be used with caution. Results like these are useful for validation of e.g. detonation simulations, but this is outside the scope of this study. It was noted that S2 failed in some cases, which makes the redundancy setup useful.

6. Series 3 – P400 versus R400

6.1. Setup of series 3

Fig. 14 shows that sensor S8 in these tests was mounted 150 mm from the mouth of the pipe because of the flange. Apart from that and the

concrete pipe geometry, the setup of series 3 was identical to that of series 2. All data from these tests has been listed in Tables 4 and 5.

6.2. Test results of series 3

The 50 g charge for the P400-VI pipe was insufficient to breach the pipe. No surface damage was noted either. Increasing the charge size to 65 g (P400-X) caused the blast load to split the pipe in two halves of roughly equal size (see Fig. 15(a)). A charge size of 75 g produced similar results, but with more fragmentation as shown in Fig. 15(b). The 75 g test was repeated and yielded exactly the same results. This damage pattern is notably different compared with the P200 pipes, where fragmentation occured for the lowest charge breaching the pipe. While the D_i/t_w ratio is quite similar for the two geometries, the ℓ/D_i ratio is higher for the P200 pipes. The longer ℓ compared with D_i seems to prohibit the P200 pipes from cracking at the ends while the P400 pipes do. For a full-scale SFTB, the ℓ/D_i ratio will be much higher.

A 100 g charge (P400-V) broke the pipe into large pieces with

Table 5
Experimental matrix and results for reinforced concrete pipes in series 3 sorted by charge size.

parameter	unit	R400-II		R400-III		R400-IV		R400-IX		R400-XII		R400-XI	
R	[mm]	200		200		200		200		200		200	
W	[g]	150		200		300		400		400		500	
Z	[m/kg$^{1/3}$]	0.376		0.342		0.299		0.271		0.271		0.252	
$\bar{a}$	[cm]	69±23		97±17		119±31		129±26		146±43		150±53	
a_{max}	[cm]	100		124		167		183		235		235	
P_1/P_4	[kPa]	1293	1123	2561*	1429	2559*	2545*	2557*	2542*	–	–	2559*	2543*
P_2/P_5	[kPa]	–	717	–	827	–	2553*	–	1398	–	–	1956	1592
P_3/P_6	[kPa]	237	187	299	246	855	871	439	871	–	–	557	1022
P_7	[kPa]	–		–		3129		5152		–		1947	
P_8	[kPa]	2567		2797		5125		4696		–		4700	
t_1/t_4	[ms]	0.79	0.80	0.73	0.71	0.66	0.66	0.62	0.61	–	–	0.54	0.65
t_2/t_5	[ms]	1.15	1.19	1.07	1.06	0.94	0.94	0.87	0.86	–	–	0.77	0.91
t_3/t_6	[ms]	2.25	2.34	2.08	2.11	1.82	1.83	1.68	1.69	–	–	1.51	1.71
t_7	[ms]	–		–		0.38		0.36		–		0.31	
t_8	[ms]	0.53		0.50		0.44		0.41		–		0.36	
i_1^+/i_4^+	[kPa·ms]	398	316	481	360	655	536	694	581	–	–	821	588
i_2^+/i_5^+	[kPa·ms]	–	200	–	243	–	358	–	366	–	–	490	391
i_3^+/i_6^+	[kPa·ms]	133	124	145	133	183	181	168	182	–	–	201	196
i_7^+	[kPa·ms]	–		–		856		390		–		521	
i_8^+	[kPa·ms]	1063		1442		1756		1980		–		–	
t_1^+/t_4^+	[ms]	1.15	0.75	1.34	0.81	1.40	0.93	1.65	0.86	–	–	1.77	1.14
t_2^+/t_5^+	[ms]	–	1.86	–	2.07	–	2.02	–	2.35	–	–	2.52	2.82
t_3^+/t_6^+	[ms]	2.72	2.94	2.46	2.64	2.48	2.61	1.75	1.82	–	–	1.72	1.75
t_7^+	[ms]	–		–		0.82		0.23		–		0.55	
t_8^+	[ms]	3.43		3.83		3.78		3.66		–		–	
v_{07}	[m/s]	–		–		2434		2569		–		2984	
v_{08}	[m/s]	1934		2050		2330		2500		–		2847	
v_{78}	[m/s]	–		–		1667		2000		–		2000	
v_{12}/v_{45}	[m/s]	1111	1026	1176	1143	1429	1429	1600	1600	–	–	1739	1538
v_{23}/v_{56}	[m/s]	727	696	792	762	909	899	988	964	–	–	1081	1000

*The sensor recording range was saturated, which means that the peak pressure was higher than this number.
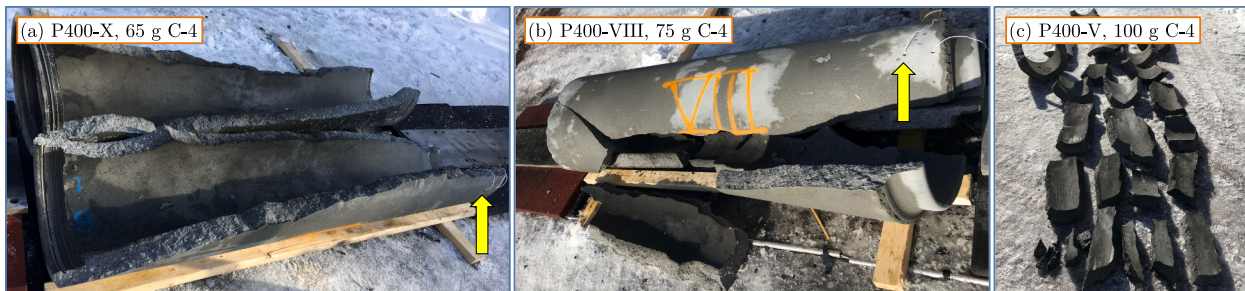

Fig. 15. Post-test photographs of plain concrete pipes, (a) P400-X 65 g, (b) P400-VIII 75 g and (c) P400-V 100 g.

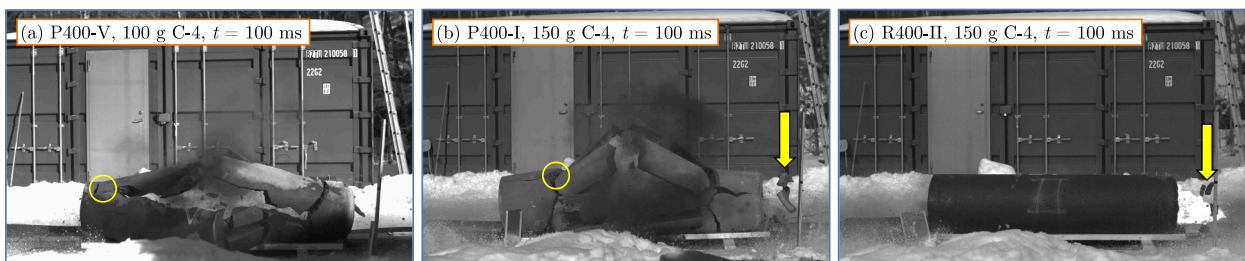**Fig. 16.** Images from high-speed videos at $t = 100$ ms of (a) 100 g C-4 in P400 pipe, (b) 150 g C-4 in P400 pipe, and (c) 150 g C-4 in R400 pipe.
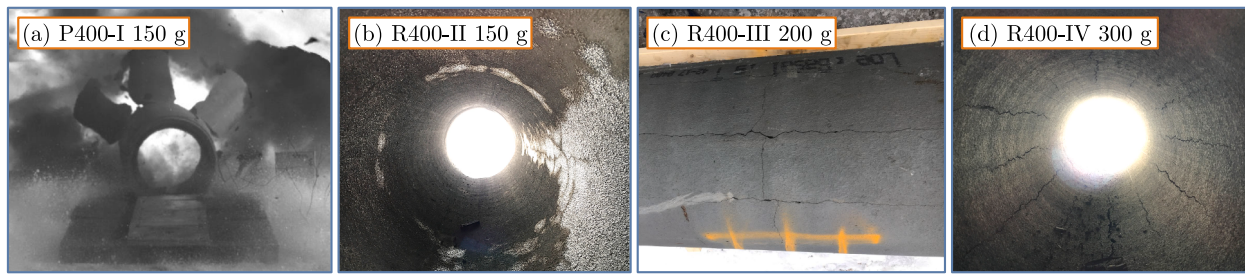
Fig. 17. Typical fracture patterns from series 3 where (a) shows pipe P400-I 77 ms after detonations, while (b), (c) and (d) show pipe R400-II, R400-III and R400-IV post-testing.
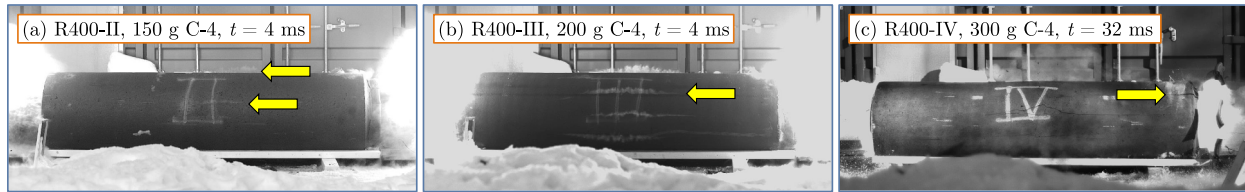

Fig. 18. Images from high-speed video of (a) R400-II 150 g, (b) R400-III 200 g and (c) R400-IV 300 g.

longitudinal cracks running almost the entire length of the pipe, depicted in Figs. 15(c) and 16(a). For this pipe, a crack ran through the holes for sensors S7 and S8, but this was the only P400 pipe where this happened and is most likely coincidental. For 150 g of C-4, smaller and more fragments were produced than for 100 g and the fragments formed as shown in Fig. 16(b). Note that the inflection point for the formation of fragments is closer to the centre for 150 g than for 100 g, indicated by the yellow circles in Fig. 16. Large charge sizes tend to produce more local punching failure than small charge sizes detonated from the same standoff distance [57], an effect which is seen both here and in the previous test series. Increasing the charge size beyond 150 g would undoubtedly result in even more and smaller fragments in accordance with the observations from the previous series. In addition, the connecting flange of pipe P400-I broke off in the wall thickness transition area in one end (look below the arrow in the right part of Fig. 16(b)). This result is most likely caused by stress waves travelling and reflecting inside the pipe wall. Measuring the average crack length $\bar{a}$ for the plain concrete pipes was not very useful, because the pipe either remained intact or broke into several pieces along the entire length. This never happened to the smaller pipes, indicating some size effects as mentioned.

Fig. 16(c) shows reinforced pipe R400-II during testing, where the connecting flange broke off like for the plain concrete pipe P400-I subjected to the same charge size (150 g). This did not happen for the 100 g charge for pipe P400-V, which means that this phenomenon depends on the magnitude of the load. The 150 g charge broke the plain concrete pipe P400-I into several pieces in a petalling formation as shown in Fig. 17(a), while the reinforced pipe appeared to suffer only

surface cracks. Cracks as seen from the inside of the pipe are shown in Fig. 17(b). Judging from the high-speed image in Fig. 18(a), the cracks may have extended through the wall thickness of pipe R400-II because dust was observed escaping from where the cracks formed (look near the arrows in Fig. 18(a)). The dust could, however, also have been formed from the generation of new free surfaces inside the concrete, so the cracks do not necessarily extend through the thickness. The dust cloud was also relatively small compared with the very clear dust lines seen for pipe R400-III (200 g) in Fig. 18(b).

A charge size between 150 g and 200 g C-4 is probably sufficient to generate through-thickness cracks for the reinforced concrete pipes used herein. Given the external cracks (shown for R400-III in Fig. 17(c)) and their general alignment with the internal cracks (shown for R400-IV in Fig. 17(d)), the detachment of fragments from the pipe, and the cracks running through the thickness at the end of the pipe (near the arrow in Fig. 18(c)), it was concluded that the cracks ran through the entire pipe wall thickness for charge sizes of 200 g and above. It was clear that 300 g created through-thickness cracks. This shows just one example of the importance of the choices in terms of thickness of the cross-section and of the reinforcement that the designers must take into consideration. The average and maximum crack lengths along the reinforced pipes ($\bar{a}$ and $a_{\max}$ respectively) increased with increasing charge size as expected (see Table 5). The crack width also increased, from at most 2 mm for pipe R400-II to about 5 mm for pipe R400-IV (plus detaching fragments). For pipe R400-IV, a crack formed through both holes for pressure sensors S7 and S8. This did not happen for any of the other reinforced pipes.

The pressure recordings were generally in accordance with expectations, and scales reasonably with the recordings from series 2. An
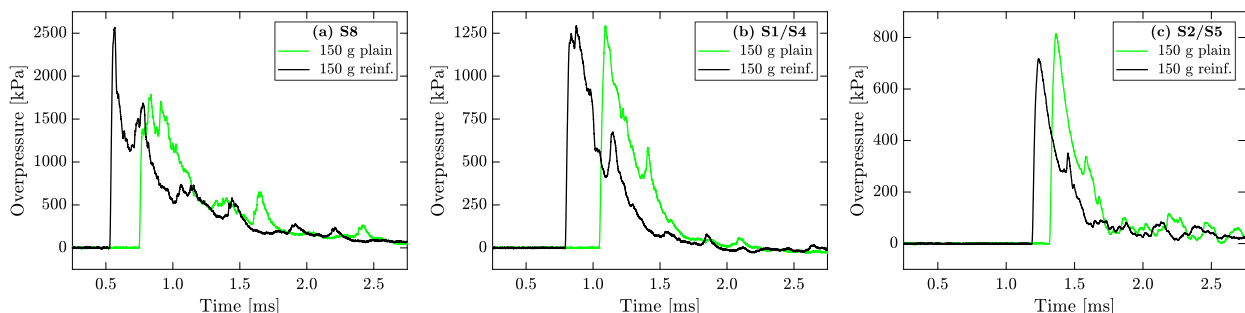

Fig. 19. Pressure data from (a) sensor S8, (b) sensor S1/S4 and (c) sensor S2/S5 for tests of P400 pipe and R400 subjected to a 150 g charge.
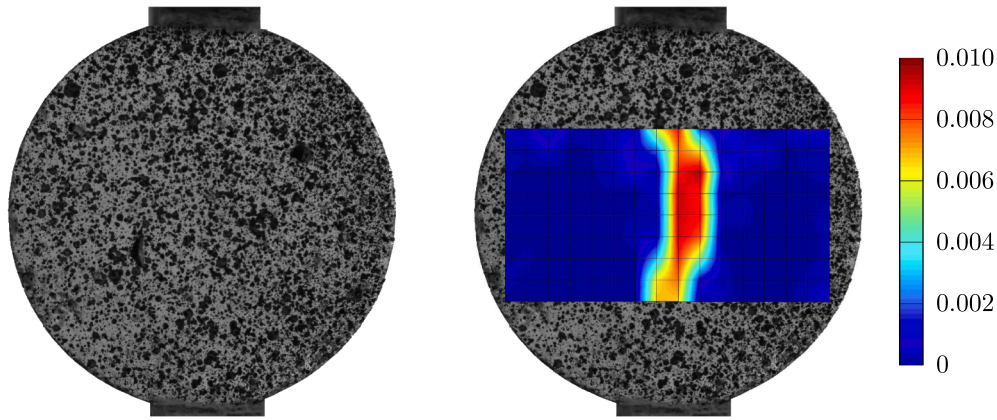
Fig. 20. An image from a tensile splitting test (left) with a contour plot of the major principal strain from the DIC analysis (right).

example from series 3 is shown for the overlapping charge (150 g) in Fig. 19. The arrival time is higher for the plain pipe because some energy goes into fragmenting the pipe. It is interesting to note that the magnitude of the pressure is approximately the same in Fig. 19(a) as in Fig. 13 (a) and (b). The scaled distance Z from Eq. (1) is approximately 2 m/ $\mathrm{kg}^{1/3}$ in both cases, thereby indicating some validity for the scaling law even for confined detonation [50]. The remainder of the data sets are included in Appendix A. Sensors S1 and S4 were saturated in several tests as shown in Table 5, and the real pressure is somewhat higher than what is listed there.

7. Finite element simulations

All finite element simulations were carried out using the explicit nonlinear FE solver IMPETUS AFEA Solver [58]. The solver offers e.g. GPU acceleration, fully integrated higher order Lagrangian volume elements, and node splitting to describe fracture [59]. With higher order elements it is possible to represent a curved surface accurately, which is highly beneficial for the cylindrical test specimens and the tubular concrete structures.

7.1. Calibration of the concrete material model

The material tests from Section 2.1 were used for calibration of the material model. All the concrete specimens were as mentioned painted with a speckled pattern for use with the finite element-based DIC software eCorr [42]. An example image from a tensile splitting test is shown in Fig. 20, where the left part shows an image from the test and the right part shows the same image with the calculated major principal strain field from the 2D-DIC results superposed. The rapid increase in strain in the centre indicates that a crack is forming. It is interesting to note that DIC is able to pick up the crack location before it is visible to the naked eye in the image.

For the calibration, the DIC results were used to estimate the compressive or tensile engineering strain directly on the specimen by measuring the shortening or elongation of vectors spanning across the

test specimen. This data, together with the force logged from the load cell, were used as target curves for an optimisation procedure to determine the material constants by inverse modelling of the tests. Mesh sensitivity is naturally an important issue for concrete exposed to extreme loadings [60]. Here, a computational cell approach was used to handle the mesh size dependency [61], where the same element size (20 mm) was used in the calibration simulations as in the simulations of the component tests.

The IMPETUS AFEA concrete model [58] has been applied successfully to blast loading of concrete structures (for instance to the full-scale blast experiments by Heggelund et al. [62]). The model has different failure mechanisms in compression and tension, the shear resistance is considered pressure dependent, and inelastic dilatation (interpreted as crushing) reduces this shear resistance. Deviatoric inelastic strains above a critical value result in macroscopic cracking, which is represented by node splitting. The model accounts for strain rate sensitivity, but only quasi-static material tests were conducted in this study. For this reason the default values of the strain rate parameters were used [58]. Further details on the material model have been included in Appendix B.

An LS-OPT [63] procedure was set up to obtain the material parameters through inverse modelling. 64-node fully integrated cubic elements were used to discretise the specimens for the computational cell approach, and the element side lengths were approximately 20 mm. A time scaling factor of 10^{-2} was used to reduce the simulation time, and all three strain rate parameters were set to zero. For the blast simulations, default values for these parameters were used (see Table 6). Contact between the compression plates and the specimen was ensured by a penalty approach with a friction coefficient of $\mu = 0.47$ [64]. The compression plates were modelled as rigid and the geometry was adapted to mimic the experimental conditions. The mesh for each test specimen is shown in Fig. 21, where (b) and (c) illustrate the ability of the higher order elements to represent curved surfaces. The thick mesh grid lines indicate element boundaries, while the thin lines represent the internal node grid of each element.

The results in terms of engineering stress–strain curves are also shown in Fig. 21. The cylinder compression test was used as the

Table 6
Material parameters for the IMPETUS AFEA concrete model described in Appendix B.

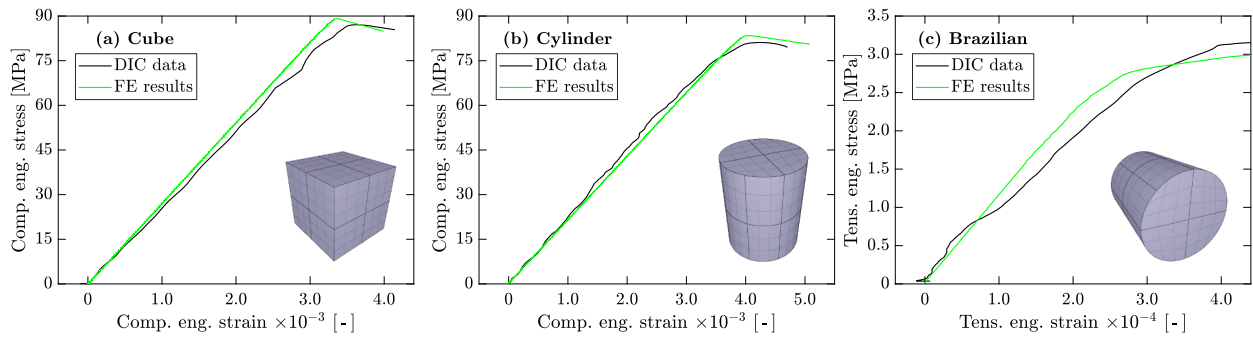| Obtained	Parameters, units and values							
Tests	ρ [kg/m^3]	f_c [MPa]	f_t [MPa]					
	2440	76.1	3.2					
LS-OPT	G [GPa]	ε_c [–]	ε_t [–]	K_0 [GPa]	K_L [GPa]	p_0 [MPa]	p_L [MPa]	ε_L [–]
	4.96	0.021	0.002	6.62	10.58	121.8	812.3	0.070
Default	r_s [kPa·s]	r_p [kPa·s]	c [kPa·s]	ξ [–]	n [–]			
	46	2000	500	0.80	2.0			

Fig. 21. Estimated engineering stress–strain curves from tests and simulation for (a) cube compression test, (b) cylinder compression test, and (c) tensile splitting (Brazilian) test.
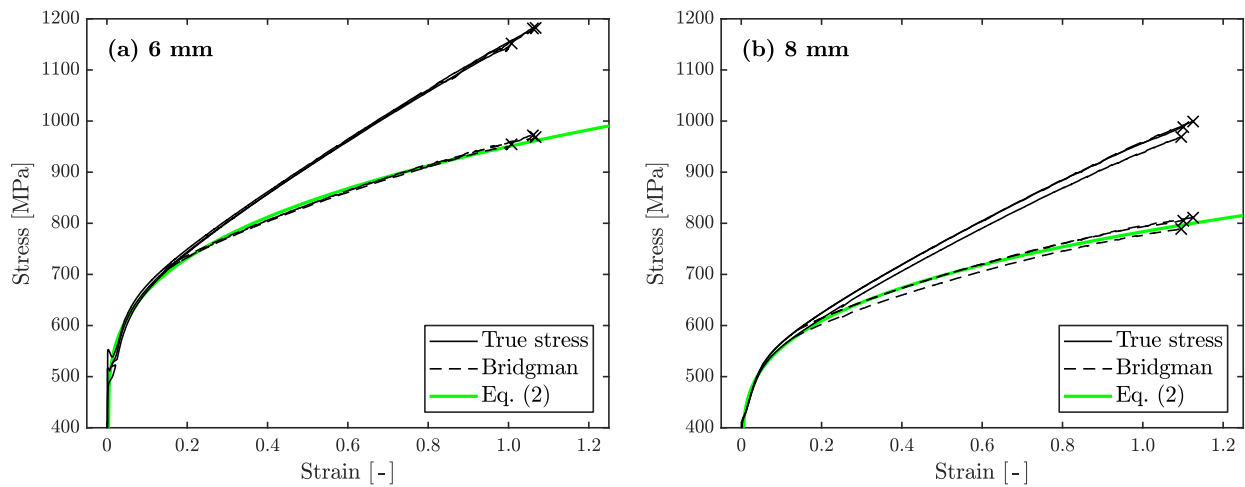

Fig. 22. Quasi-static calibration results of material model for reinforcement bars from (a) hoop and (b) longitudinal direction.

Table 7
Material parameters for the steel plasticity model.

	A [MPa]	B [MPa]	N [–]	C [–]	$\dot{\varepsilon}_0$ [1/s]
6 mm (hoop)	425.6	525.2	0.331	0.010	10^{-3}
8 mm (longitudinal)	350.5	433.7	0.317	0.010	10^{-3}

calibration target, while the cube compression test and Brazilian test were used for validation. The latter had a slightly higher deviation because of the relatively larger scatter in these tests, but the simulation results were still well within the experimental range. In general, the results are very good and the parameters obtained should be able to represent the material at this scale. The kinetic energy was less than 2 % in all simulations, indicating quasi-static loading conditions. All concrete material parameters are given in Table 6, sorted by how they were obtained. An explanation of all the parameters and the model can be

found in Appendix B.

7.2. Reinforcement material model

The reinforcement was modelled by 2-node beam elements with an element size of 10 mm. The mass density and Young's modulus used were 7800 kg/m^3 and 210 GPa, respectively. Conventional J2 plasticity was used for the steel, with power law strain hardening and multiplicative strain rate sensitivity on the following form:

$$\sigma_{\text{eq}} = \left(A + B\varepsilon_{\text{eq}}^N\right)\left(1 + \frac{\dot{\varepsilon}_{\text{eq}}}{\dot{\varepsilon}_0}\right)^C \tag{2}$$

where $\sigma_{\text{eq}}, \varepsilon_{\text{eq}}$ and $\dot{\varepsilon}_{\text{eq}}$ are the equivalent stress, equivalent strain and equivalent strain rate, respectively. A, B, N and C are material parameters, while $\dot{\varepsilon}_0$ is the reference strain rate at which the quasi-static tests were performed. A, B and N were found by Bridgman correcting [65] the
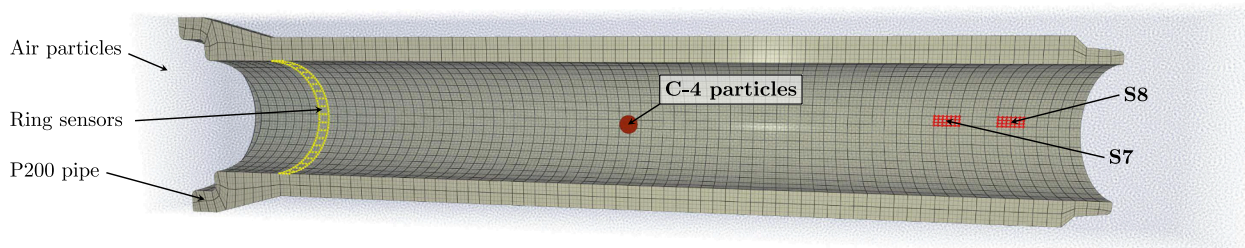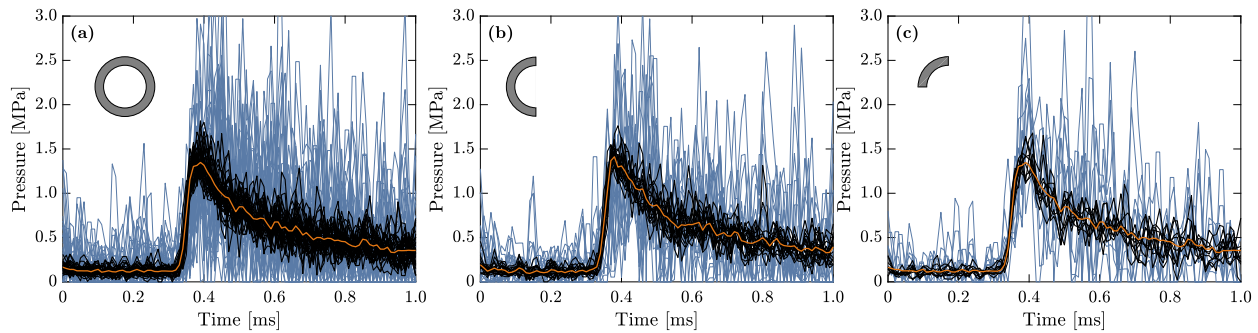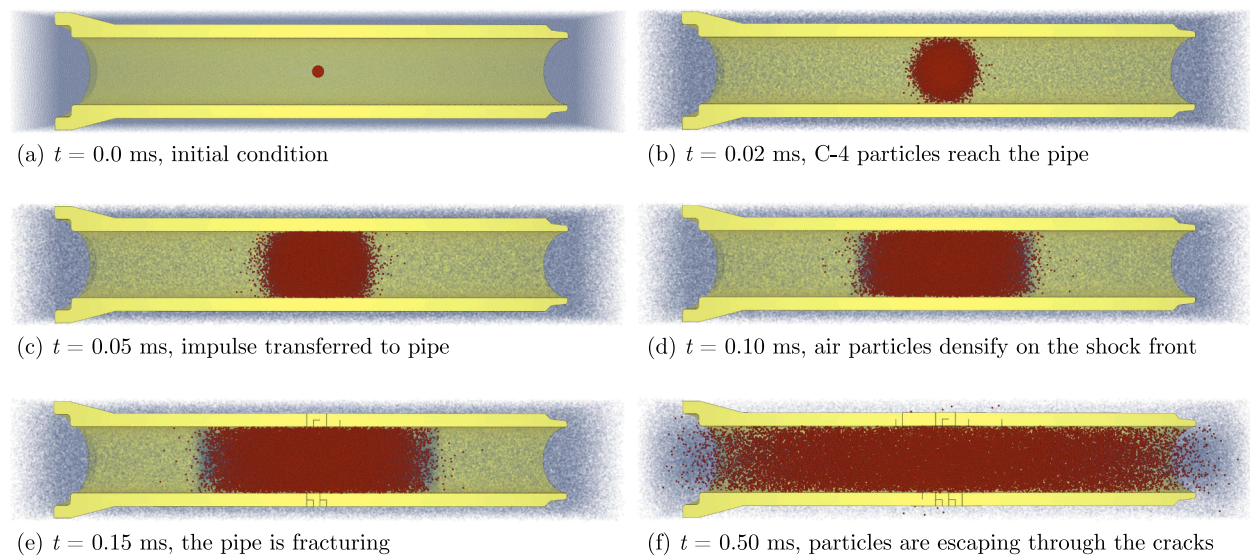

Fig. 23. The setup for the half symmetric numerical model of P200 concrete pipes.

Fig. 24. Pressure–time curves from the "ring sensors" for a charge size of 15 g for (a) full pipe, (b) half symmetry and (c) quarter symmetry. The blue lines arise from using 100 000 particles and the black lines from using 1 000 000 particles, while the orange curves are the average of the black lines for each plot.

(a) $t = 0.0$ ms, initial condition

(b) $t = 0.02$ ms, C-4 particles reach the pipe

(c) $t = 0.05$ ms, impulse transferred to pipe

(d) $t = 0.10$ ms, air particles densify on the shock front

(e) $t = 0.15$ ms, the pipe is fracturing

(f) $t = 0.50$ ms, particles are escaping through the cracks

Fig. 25. Time lapse of simulations of half symmetric P200 pipe subjected to a 25 g C-4 charge.

curves in Fig. 3 and finding a least squares fit for both reinforcement steels as plotted in Fig. 22 and listed in Table 7. The strain rate sensitivity parameter C was chosen based on previous work on high rate loading of steel [66,67]. No fracture criterion was used because the reinforcement did not fracture in any of the experiments.

7.3. Preliminary blast simulations

It is important to account for the confinement arising from detonating the charge inside the pipe [68]. For this reason, a discrete particle method was used to describe the blast load [69,70] in a purely Lagrangian formulation. This approach uses particles and transfer of momentum to the structure to represent the blast load. The effect of confinement is thus included by construction, and all considerations required to properly handle the fluid–structure interface [71] are bypassed. The drawback is that the negative phase of the load is not included, but for stiff structures with small deformations, this is not critical [43]. First, a preliminary study was conducted to determine the number of particles required and to investigate whether symmetry is applicable. The setup for a half symmetric model is shown in Fig. 23. A quarter symmetry model and full model were also used. Fully integrated 64-node cubic elements with side lengths 20 mm were used for the pipe. The number of elements for the full P200 pipe was 6 480, and the number of nodes was 414 720. The air particle domain encompasses the pipe and extends beyond both pipe ends to allow particles to flow out.

The domain measures 370 mm $\times$ 370 mm $\times$ 1870 mm for the full model, and the charge is placed in the centre of the domain. Particles exiting the domain are deleted from the analysis. Contact between the particles and the pipe is enforced by the penalty method with a friction coefficient of 0.4 to account for the rough surface of the concrete. The same approach was used for the self-contact between the pipe fragments.

The element faces labelled "Ring sensors" in Fig. 23 were used to check whether the pressure was approximately homogeneous around the circumference. If too few particles are used, there will be a larger scatter for the pressure–time curves which might not resemble a blast load profile anymore. The ring sensors were also used to make sure that symmetry was retained for half and quarter symmetry models. The black lines in Fig. 24(a) show the pressure–time history[1] for each element surface in the ring when using 100 000 particles for the full pipe (50 000 and 25 000 for the half and quarter symmetric models in (b) and (c), respectively). Using 100 000 particles results in a large range of scatter, and a severely non-homogeneous pressure distribution across the circumference. Increasing the number of particles to 1 000 000 reduces this effect significantly. The same applies to the half and quarter symmetric models. Increasing the particle count even further smoothened

---

[1] The software measures the total impulse transferred to each element, and the pressure–time history is obtained by differentiating this impulse with respect to time.
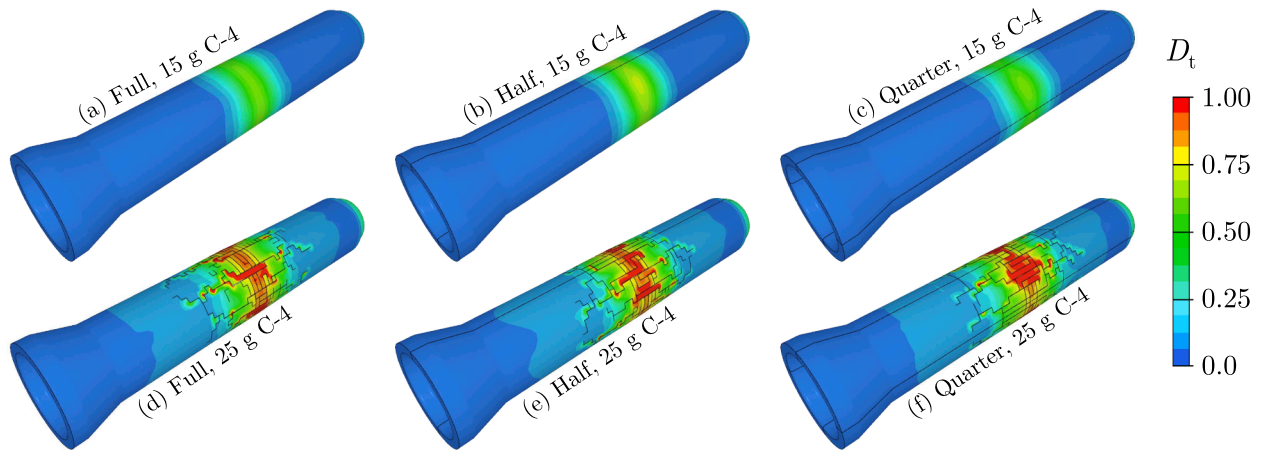
Fig. 26. An overview of the tensile damage D_t in a P200 pipe after 1.00 ms simulation time for different symmetries (none, half and quarter) and for charge sizes of 15 g and 25 g C-4 detonated from position (i). Node splitting is clearly seen as black lines for the 25 g charge simulations (do not confuse with symmetry lines).
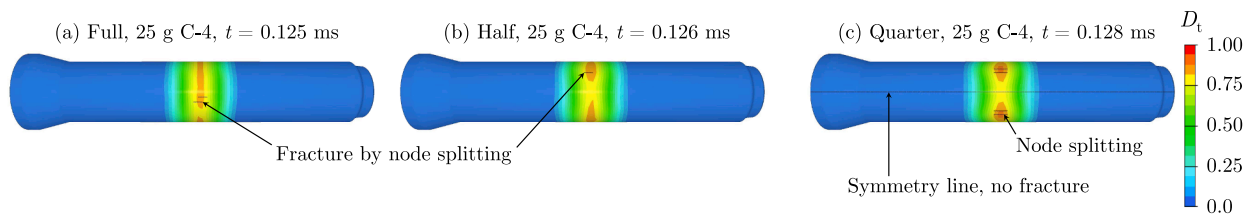

Fig. 27. The tensile damage D_t in a P200 pipe at first fracture for the different symmetries (a) none, (b) half and (c) quarter, for a charge size 25 g C-4 detonated from position (i).

the pressure–time histories more, but it was decided to leave the number at 1 000 000 to keep the computational time reasonable. A time lapse of a half symmetric P200 pipe using 1 000 000 (meaning 500 000 for the half model) is shown in Fig. 25. A quick comparison of the experimental data from S7 and S8 with the numerical data shows that the simulations slightly underpredict the measured pressure and impulse while the arrival times are quite close. Making a proper validation of the described load like in e.g. [72] requires additional tailored experiments and simulations and is thus therefore left for further work.

Now that the pressure has been shown to be symmetric and reasonably close to the experimental data for 1 000 000 particles, it is now time to investigate whether the structural response is adequately captured by the symmetric models. Globally, the simulation outcomes are quite similar between the various symmetries as shown in Fig. 26 for a 15 g charge and a 25 g charge detonated from position (i). This result means that symmetry is applicable if a global estimate is needed. Still, the pipe did not break for the 15 g charge for any of the cases even though 13 g was sufficient in the experiments. The damage variable D_t was approximately 0.9, where $D_t = 1.0$ give fracture by node splitting. For comparison, a simulation of the full pipe exposed to a 15 g charge detonated from position (i) was run without accounting for strain rate sensitivity, i.e., setting r_s, r_p and c equal to zero. In this case, the pipe fragmented completely, thereby confirming the need to account for the

strain rate which in these simulations typically exceeded 1 000 s^{-1}. Proper strain rate data could help improve the FE results since this may have a significant influence on the results [22].

On a local level there are some differences as highlighted in Fig. 27. The figure shows the P200 pipe at first fracture for the three symmetry cases. Here, fracture initiates after 0.125 ms, 0.126 ms and 0.128 ms for the full, half and quarter symmetric models, respectively. The damage pattern for the quarter model is a bit different, but good global estimates are still achieved. The fracture pattern is naturally more restricted for the models using symmetry, but the representation still looks realistic in Fig. 26. In all simulations, the fracture starts as longitudinal cracks that propagate and connect to form fragments – exactly as in the experiments. The momentum of the particles cause the fragments to detach from the main body of the pipe by node-splitting. This is difficult to achieve by applying a pressure–time load like CONWEP in combination with element erosion [49] in stead of node splitting. So for global evaluations like here, symmetric models are in general valid, while for more detailed behaviour like crack initiation and propagation, a full model – ideally with a fine mesh – is preferable.

7.4. Contact charge simulations

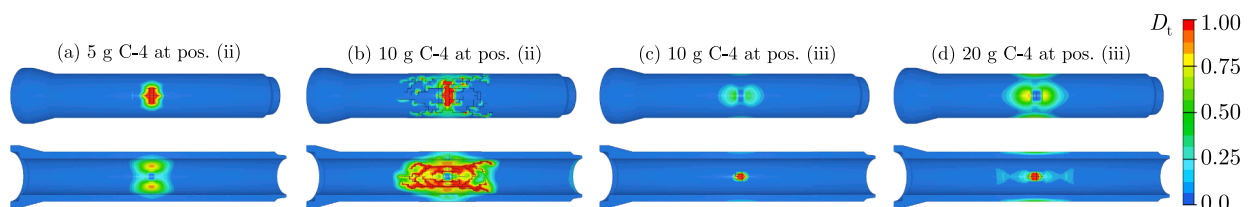Contact detonations and their consequences can be difficult model

Fig. 28. Results after 1.0 ms simulation time of contact charge at position (ii) and position (iii).
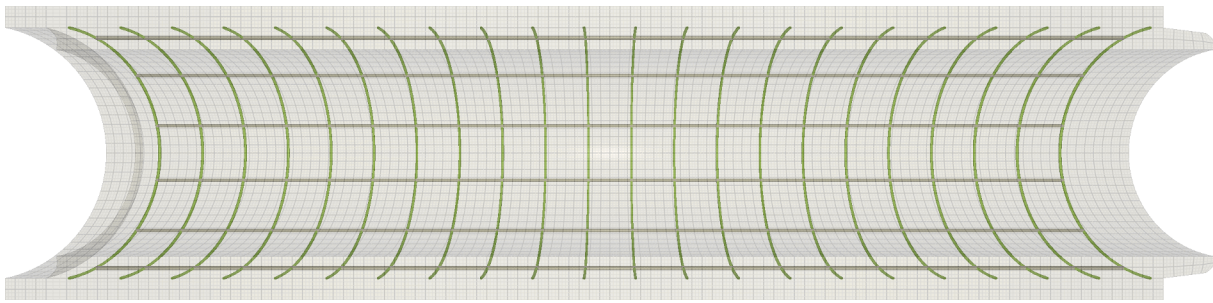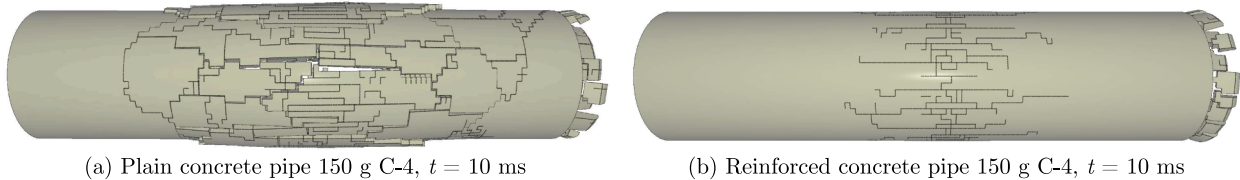
Fig. 29. Mesh for P400 (plain concrete) and R400 (reinforced) pipes.

(a) Plain concrete pipe 150 g C-4, $t = 10$ ms

(b) Reinforced concrete pipe 150 g C-4, $t = 10$ ms

Fig. 30. Comparison of simulation results from a half symmetric model of (a) P400 plain concrete pipe and (b) R400 reinforced pipe subjected to an internal detonation of 150 g C-4.

accurately, and the choice of modelling strategy is important [73]. Here, the goal to investigate if the current modelling strategy with particles is a viable approach (no symmetry utilised). The approach was exactly as in Fig. 23, but rather than a spherical charge in the centre of the pipe a cubic contact charge as in Fig. 5 is modelled. No special actions were taken other than this. Both contact positions were modelled, (ii) internal and (iii) external. Since the element size was 20 mm, a comparison of crater and hole size was not practicable.

Qualitatively, the numerical results in Fig. 28 were in good agreement with the experiments. The maximum damage was always on the opposite side of the charge like the tests in series 1, and the internal charge (ii) produced significantly more damage than the external (iii). The quantitative results were also close to the experiments. The internal 5 g charge did not produce through-thickness cracks, and the most damaged area was exactly where the scabbing occured in the tests due to reflection of stress waves at the opposite surface. The internal 10 g charge clearly produced fragments and a large area was damaged in the pipe (Fig. 28(b)). A 10 g charge on the outside, however, did not produce anywhere near the same amount of damage. While the 10 g charge at (iii) did produce some cracking on the inside of the pipe in Fig. 28(c), there was no through-thickness cracking. For the 20 g charge through-thickness cracks were noted, shown in Fig. 28(d). These results correspond well with the experiments, both qualitatively and quantitatively.

7.5. P400 and R400 pipes

Simulations of the 400 mm diameter pipes with and without reinforcement, i.e., R400 and P400, were also conducted. The reinforcement mesh is simply superposed with the concrete mesh, and a perfect bond between the steel and concrete is assumed. For simplicity and compatibility with symmetry, the hoop reinforcement bars were represented by circles rather than a continuous dodecagon helix, shown for the half symmetric model in Fig. 29. The number of elements for the full P400 pipe was 30 600, and the number of nodes was 1 959 544. For the full reinforcement, there were 2910 elements and 2944 nodes. The air particle domain for the full model now measures 740 mm × 740 mm × 2820 mm, so to keep the same particle density per unit volume the number of particles was increased by a factor of 6.

A charge size of 150 g was used since both plain concrete and reinforced concrete pipes were tested for this charge. As seen from Fig. 16(b) and (c), the P400-I pipe was destroyed while the R400-II pipe only

suffered surface cracks and possibly a few through-thickness cracks. The simulation results in Fig. 30(a) and (b) largely replicate this behaviour. Even the connecting flange detaches exactly like in the experiments, and the reinforcement bars act like crack indicators as seen before in simulations of reinforced concrete [43]. The average and maximum crack lengths $\bar{a}$ and $a_{\max}$ were 61 cm and 87 cm for the simulation in Fig. 30(b), while the corresponding experimental values were 69 cm and 100 cm. This direct comparison is not entirely accurate, because running the simulation to e.g. 20 ms rather than 10 ms will increase these values somewhat. That would, however, approximately double an already long simulation time of 37.5 h. Like for the P200 simulations, a larger charge size than the experimental value was needed to breach the pipe. A simulation of a P400 pipe subjected to 100 g C-4 did not breach the pipe after 10 ms simulation time, while 125 g did. Altering the friction coefficient between the particles and the pipe might improve this result. Improving the quantitative accuracy of the simulations further can be done by obtaining material data at elevated strain rates, and validate the description of the load more rigorously.

8. Concluding remarks

The two main goals of this study were to establish an elaborate experimental database for blast loading of tubular concrete structures, and to investigate how well commercial finite element simulations are able to represent the experiments.

The first goal was met through blast load testing of mass produced concrete pipes with various configurations. The charge size needed to breach a 200 mm internal diameter plain concrete pipe was determined from three positions: (i) centrically placed, (ii) contact inside and (iii) contact outside. The tests showed a significant confinement effect, where a contact charge detonated from the outside required twice the explosive mass to breach the pipe compared with a contact charge detonated from the inside. It was also shown that the pressure inside the pipe appears to be notably higher than the pressure immediately outside the pipe, underscoring the confinement. This effect needs to be accounted for if this type of structure were to be built. Pressure sensors with roughly equal scaled distance from the charge gave similar pressure recordings, indicating validity for the Hopkinson-Cranz scaling law. Larger charge sizes generally produced lower arrival times and higher shock wave velocities. To no surprise, adding reinforcement improved the blast resistance substantially. Besides adding more reinforcement,

tunnel linings can be used to mitigate the blast load [74] and should at least be applied in the zones where the floating pontoons or tethers are located [75]. Steel jackets and polyurethane are alternative solutions [76].

The finite element simulations generally gave good results. A concrete material model was calibrated based on inverse modelling of quasi-static material tests. Digital image correlation was used to obtain strain data locally on the specimen surface. Higher order elements were used to represent the curved surface of the cylindrical specimens and the pipes in the blast simulations. For the particle blast method to work well, a critical number of particles is required to emulate a blast-like loading. This number increases when the element size decreases. The charge size needed to breach the pipe was slightly higher in the simulations than in the tests – a result which is non-conservative. Using symmetry was shown to work well for a global estimate, but if crack initiation and propagation is of interest a full model should be used. Discrete particles appear to work very well for modelling a contact charge – all the key observations from the tests were reproduced without making any special considerations for the contact. In general, a higher charge mass was needed in the FE simulations to breach the pipe compared with the tests, which might be explained by the slightly underpredicted load. The importance of including strain rate sensitivity in this type of simulation was shown by excluding such effects from one simulation where the pipe initially remained intact. This resulted in complete destruction of the pipe. The effect of the reinforcement was also captured adequately.

To improve the results and to gain a better understanding of the observations, a thorough load characterisation should be carried out in a confined environment. This would help quantify the confinement effect and give a description of the blast wave propagation and magnitude – important data for designing tubular concrete structures like SFTBs. Repeating these tests underwater for comparison would provide additional information on how the water might affect the results. Further, material data at elevated strain rates should improve the numerical results compared with using standard values. The inhomogeneous nature of concrete is not addressed herein, but could be accounted for by mesoscale modelling [77,78] or a stochastic approach [79].

CRediT authorship contribution statement

Martin Kristoffersen: Methodology, Investigation, Conceptualization, Writing - original draft, Visualization, Formal analysis. **Knut Ove Hauge:** Investigation, Resources, Writing - review & editing. **Arianna Minoretti:** Funding acquisition, Conceptualization, Writing - review & editing. **Tore Børvik:** Supervision, Writing - review & editing, Conceptualization.

Declaration of Competing Interest

The authors declare that they have no known competing financial interests or personal relationships that could have appeared to influence the work reported in this paper.

Acknowledgements

Appendix A. Pressure recordings from series 3

The pressure recordings from test series 3 in Section 6 are included in this appendix for completeness, and are plotted in Fig. A.1 and Fig. A.2. Some of the test data from the internal sensors (S7 and S8) are somewhat unsure and should be used with caution. Note that some of the pressure recordings in Fig. A.2(c) saturated and the actual values are slightly higher.
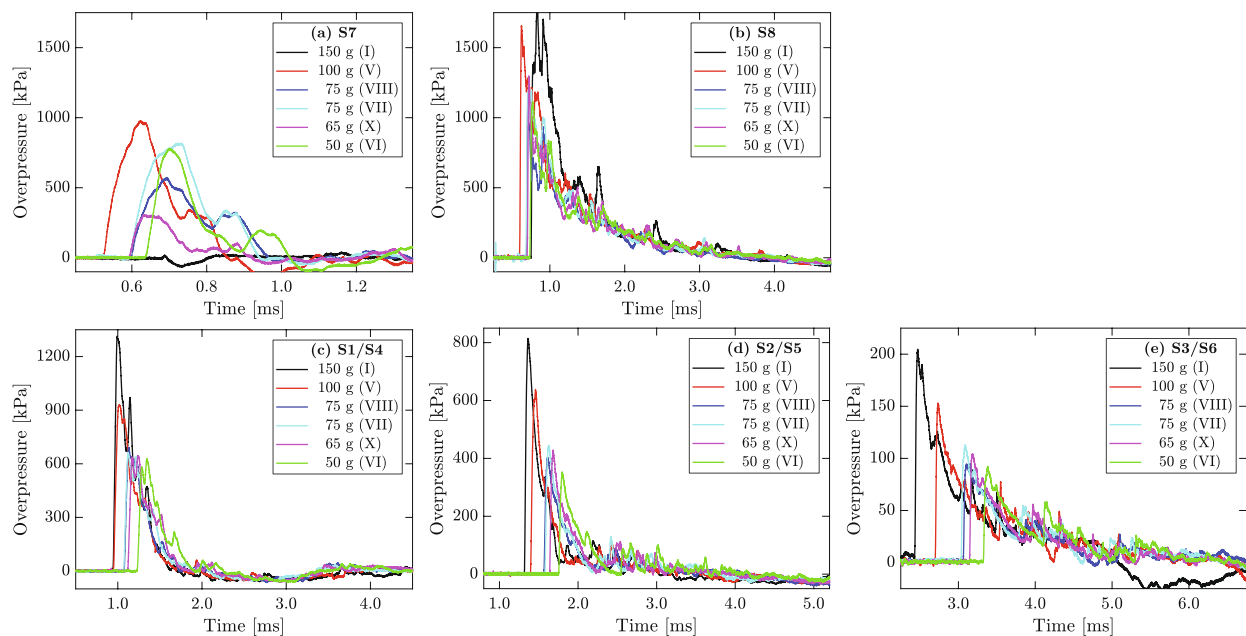

Fig. A.1. Pressure recordings from test series 3 (plain concrete pipes).
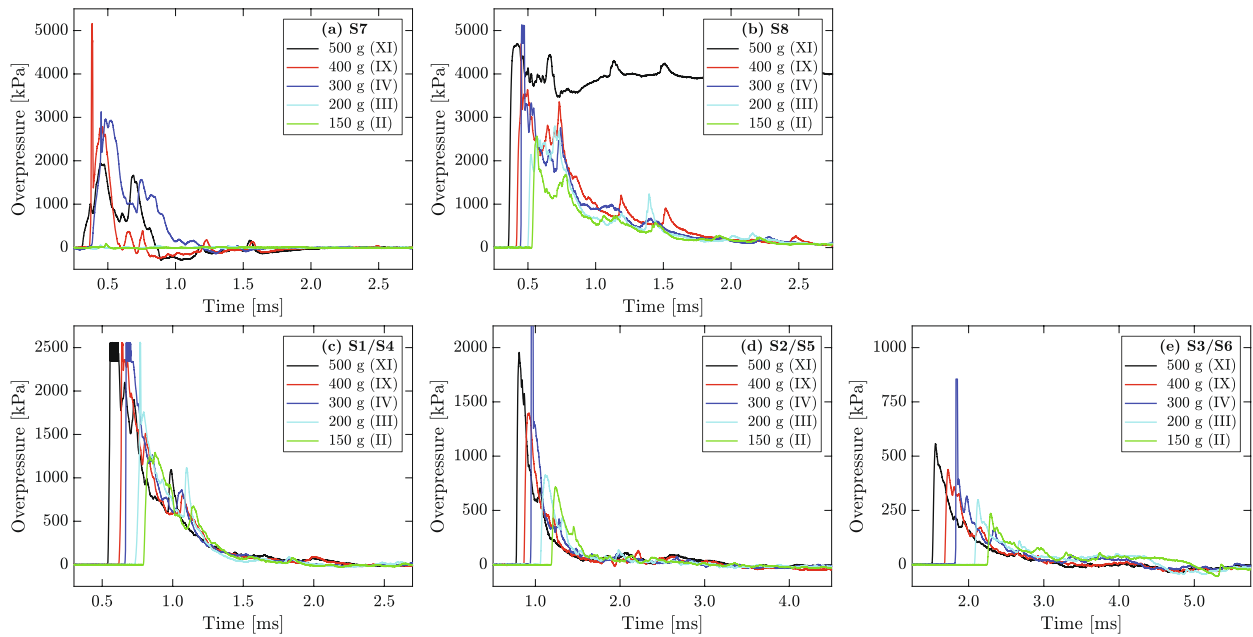
Fig. A.2. Pressure recordings from test series 3 (reinforced concrete pipes).

Appendix B. IMPETUS AFEA concrete model

The IMPETUS AFEA concrete model is described in the online documentation [58], but is briefly described here to provide an overview of the features of the model. The sum of a recoverable component $\boldsymbol{\sigma}^e$ and a viscous component $\boldsymbol{\sigma}^v$ makes up the total stress $\boldsymbol{\sigma} = \boldsymbol{\sigma}^e + \boldsymbol{\sigma}^v$. The recoverable stress component is given by

$$\boldsymbol{\sigma}^e = 2G\boldsymbol{\varepsilon}^e_{dev} - p\mathbf{I} \tag{B.1}$$

where G is the shear modulus, $\boldsymbol{\varepsilon}^e_{dev}$ is the deviatoric elastic strain tensor, p is the hydrostatic pressure (positive in compression) and $\mathbf{I}$ is the second order identity tensor. It is only $\boldsymbol{\sigma}^e$ that is used to evaluate the flow criteria in both compression and tension. The effective stress σ_{eff} is calculated from

$$\sigma_{eff} = \sqrt{\frac{3}{2}\boldsymbol{\sigma}^e_{dev} : \boldsymbol{\sigma}^e_{dev}} \tag{B.2}$$

The viscous stress component is proportional to the total strain rate $\dot{\boldsymbol{\varepsilon}}$,

$$\boldsymbol{\sigma}^v = c\dot{\boldsymbol{\varepsilon}} \tag{B.3}$$

where c is the viscosity parameter. The bulk modulus K is assumed to evolve from the initial value K_0 to K_L when the volumetric compaction strain ε_v reaches full compaction at ε_L,

$$K(\varepsilon_v) = \left(1 - \frac{\varepsilon_v}{\varepsilon_L}\right)K_0 + \frac{\varepsilon_v}{\varepsilon_L}K_L \tag{B.4}$$

Here, ε_v is the maximum inelastic volumetric strain the material has experienced. The value is always positive and can only increase, but is limited to ε_L. The compaction pressure p_c also depends on ε_v, from the initial value p_0 at the crush limit to p_L at full compaction,

$$p_c(\varepsilon_v) = p_0 + (p_L - p_0)\left(\frac{\varepsilon_v}{\varepsilon_L}\right)^n + r_p\dot{\varepsilon}_v \tag{B.5}$$

in which n determines the shape of the compaction curve. It is further assumed that p_c increases with the rate of ε_v, i.e., $\dot{\varepsilon}_v$. This effect is included additively in Eq. (B.5), and the strain rate pressure hardening parameter r_p governs this effect. The deviatoric yield stress σ_y is defined in three pressure regimes,

$$\sigma_y = \begin{cases} 0 & \text{for } p \in \langle -\infty, p_s] \\ \eta(p - p_s) & \text{for } p \in \langle p_s, \xi p_c \rangle \\ \eta(p - p_s)\sqrt{1 - \left(\dfrac{p/p_c - \xi}{1 - \xi}\right)^2} & \text{for } p \in [\xi p_c, p_c] \end{cases} \tag{B.6}$$

and is plotted in the p-σ_{eff} space in Fig. B.1(a). Here, p_c is given by Eq. (B.5) and p_s is the hydrostatic pressure cut-off, which is derived from the uniaxial tensile and compressive strengths f_t and f_c as

$$p_s = -\left(\frac{f_t \cdot f_c}{f_c - 2f_t} \cdot (1 - D_t) + \frac{r_s \dot{\varepsilon}_{\text{eff}}^p}{\eta}\right)(1 - D_c)(1 - D_0) \tag{B.7}$$

The strain rate sensitivity is included additively by the effective plastic strain rate $\dot{\varepsilon}_{\text{eff}}^p$ and the strain rate shear hardening parameter r_s. The parameter η is also derived from f_t and f_c, depends on the Lode angle $\theta \in [0°, 60°]$, and is periodic in the deviatoric plane as shown in Fig. B.1(b),

$$\eta(\theta) = \frac{3}{2} \cdot \frac{f_c - 2f_t}{f_c + f_t} \cdot \frac{1}{(1 - D_c) \cdot \cos(\theta) + D_c} \tag{B.8}$$

The Lode angle dependency for the yield surface is illustrated in Fig. B.1. The damage variables D_c, D_t and D_0 are the crushing, tensile and initial[2] damage parameters where $D_i = 0$ means no damage and $D_i = 1$ amounts to full damage. For a fully damaged material, Eq. (B.7) gives $p_s = 0$ and the Lode angle dependency disappears from η in Eq. (B.8) as illustrated in Fig. B.1(b). The volumetric crushing damage D_c is defined as

$$D_c = \min\left(1, \frac{\varepsilon_v}{\varepsilon_c}\right) \tag{B.9}$$

where ε_c is the volumetric crushing failure strain. D_t evolves by the following integral

$$D_t = \int_0^{\varepsilon_{\text{eff}}^p} \frac{1}{\varepsilon_f} \, d\varepsilon_{\text{eff}}^p \tag{B.10}$$

in which ε_f is a pressure dependent failure strain

$$\varepsilon_f = \varepsilon_t + \frac{\max(0, p)}{p_c} \cdot (\varepsilon_c - \varepsilon_t) \tag{B.11}$$

and ε_t is the uniaxial tensile failure strain. When D_t reaches unity, node splitting is activated normal to the major principal strain. The yield function f and the associated flow rule are

$$f = \sigma_{\text{eff}} - \sigma_y \leqslant 0 \qquad d\boldsymbol{\varepsilon}^p = d\lambda \cdot \frac{\partial f}{\partial \boldsymbol{\sigma}^e} \tag{B.12}$$

which allow dilatation. Integration of the plastic parameter $d\lambda$ gives the effective plastic strain

$$\varepsilon_{\text{eff}}^p = \int d\varepsilon_{\text{eff}}^p = \int d\lambda \tag{B.13}$$

Finally, the loading–unloading conditions are

$$f \leqslant 0 \qquad d\lambda \geqslant 0 \qquad f \cdot d\lambda = 0 \tag{B.14}$$

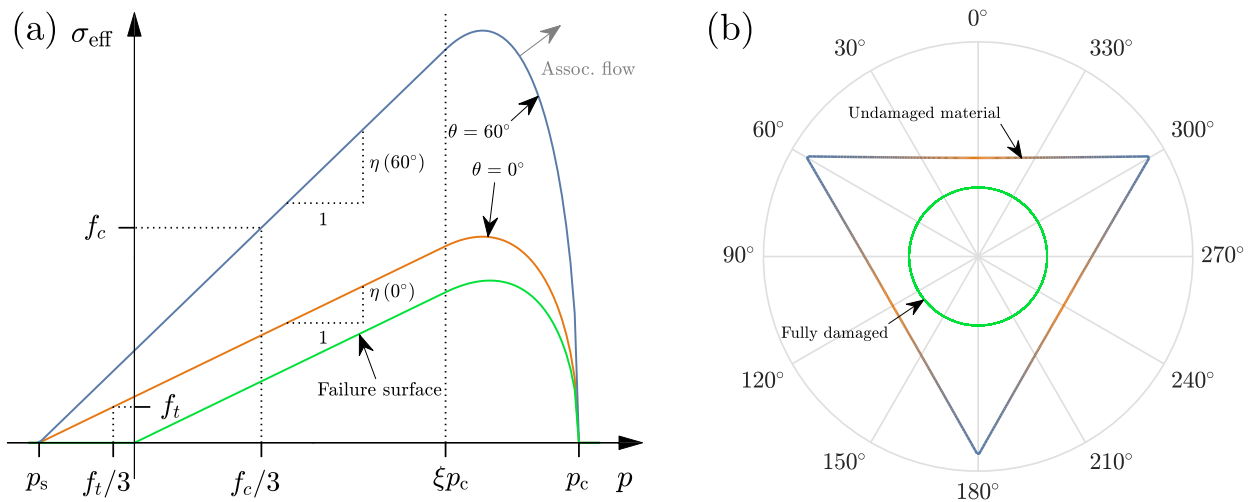[2] It is possible to add randomly distributed initial damage D_0 to a part.

Fig. B.1. The yield surface and failure surface shown in (a) the p-σ_{eff} plane, and (b) the deviatoric plane.

References

[1] Norwegian Public Roads Administration. The E39 Coastal Highway Route. 2020. http://www.vegvesen.no/Vegprosjekter/ferjefriE39/English. Accessed 24.08.2020.

[2] Minoretti A, Eidem ME, Aasland TE. The Submerged Floating Tube Bridge for the Norwegian Fjords. In: Proceedings of the 29th International Ocean and Polar Engineering Conference, Honolulu, Hawaii, USA; 2019. p. 3137–43.

[3] Larssen RM, Jakobsen SE. Submerged floating tunnels for crossing wide and deep fjords. Proc Eng 2010;4:171–8.

[4] Kanie S. Feasibility studies on various SFT in Japan and their technological evaluation. Proc Eng 2010;4:13–20.

[5] Lu W, Ge F, Wang L, Wu X, Hong Y. On the slack phenomena and snap force in tethers of submerged floating tunnels under wave conditions. Marine Struct 2011; 24(4):358–76.

[6] di Pilato M, Perotti F, Fogazzi P. 3D dynamic response of submerged floating tunnels under seismic and hydrodynamic excitation. Eng Struct 2008;30:268–81.

[7] Martire G, Faggiano B, Mazzolani FM, Zollo A, Stabile TA. Seismic analysis of a SFT solution for the Messina Strait crossing. Proc Eng 2010;4:303–10.

[8] Mazzolani FM, Landolfo R, Faggiano B, Esposto M, Perotti F, Barbella G. Structural Analyses of the Submerged FloatingTunnel Prototype in Qiandao Lake (PR of China). Adv Struct Eng 2008;11(4):439–54.

[9] Martinelli L, Barbella G, Feriani A. Modeling of Qiandao Lake submerged floating tunnel subject to multi-support seismic input. Proc Eng 2010;4:311–8.

[10] Xiang X, Eidem ME, Sekse JH, Minoretti A. Hydrodynamic loads on a sugmerged floating tube bridge induced by a passing ship or two ships in maneuver in calm water. In: Proceedings of the ASME 2016 35th International Conference on Ocean, Offshore and Arctic Engineering; 2016.

[11] Muhammad N, Ullah Z, Choi D-H. Performance Evaluation of Submerged Floating Tunnel Subjected to Hydrodynamic and Seismic Excitations. Appl Sci 2017;7:1122. https://doi.org/10.3390/app7111122.

[12] Xiang Y, Yang Y. Spatial dynamic response of submerged floating tunnel under impact load. Marine Struct 2017;53:20–31.

[13] Lin W, Xiang Y, Yang Y, Chen Z. Dynamic response analysis for submerged floating tunnel due to fluid-vehicle-tunnel interaction. Ocean Eng 2018;166:290–301.

[14] Remseth S, Leira BJ, Okstad KM, Mathisen KM, Haukås T. Dynamic response and fluid/structure interaction of submerged floating tunnels. Comput Struct 1999;72: 659–85.

[15] Mandara A, Russo E, Faggiano B, Mazzolani FM. Analysis of fluid-structure interaction for a submerged floating tunnel. Proc Eng 2016;166:397–404.

[16] Xiang Y, Chen Z, Yang Y, Lin H, Zhu S. Dynamic response analysis for submerged floating tunnel with anchor-cables subjected to sudden cable breakage. Marine Struct 2018;59:179–81.

[17] Gang L, Xiao-Jun Z, Jian-Xun C. The dynamic response of an experimental floating tunnel with different cross sections under explosive impact. J Coastal Res 2018;82: 212–7.

[18] Kristoffersen M, Minoretti A, Børvik T. Submerged floating tunnels subjected to internal blast loading. In: Proceedings of 7th Transport Research Arena TRA 2018, Vienna, Austria, 2018a. Paper no. 11360.

[19] Kristoffersen M, Minoretti A, Børvik T. On the internal blast loading of submerged floating tunnels in concrete with circular and rectangular cross-sections. Eng Fail Anal 2019;103:462–80.

[20] Schenker A, Anteby I, Gal E, Kivity Y, Nizri E, Sadot O, et al. Full-scale field tests of concrete slabs subjected to blast loads. Int J Impact Eng 2008;35:184–98.

[21] Zhang D, Yao S, Lu F, Chen X, Lin G, Wang W, Lin Y. Experimental study on scaling of RC beams under close-in blast loading. Eng Fail Anal 2013;33:497–504.

[22] Hong J, Fang Q, Chen L, Kong X. Numerical predictions of concrete slabs under contact explosion by modified K&C material model. Constr Build Mater 2017;155: 1013–24.

[23] Thai D-K, Kim S-E. Numerical investigation of the damage of RC members subjected to blast loading. Eng Fail Anal 2018;92:350–67.

[24] Krauthammer T, Bazeos N, Holmquist TJ. Modified SDOF analysis of RC box-type structures. J Struct Eng 1986;112(4):726–44.

[25] Nagata M, Beppu M, Ichino H, Takahashi J. Method for evaluating the displacement response of RC beams subjected to close-in explosion using modified SDOF model. Eng Struct 2018;157:105–18.

[26] Morales-Alonso G, Cendón DA, Gálvez F, Erice B, Sánchez-Gálvez V. Blast response analysis of reinforced concrete slabs: experimental procedure and numerical simulation. J Appl Mech 2011;78:051010.

[27] Mao L, Barnett SJ, Tyas A, Warren J, Schleyer GK, Zaini SS. Response of small scale ultra high performance fibre reinforced concrete slabs to blast loading. Constr Build Mater 2015;93:822–30.

[28] Oña M, Morales-Alonso G, Gálvez F, Sánchez-Gálvez V, Cendón D. Analysis of concrete targets with different kinds of reinforcements subjected to blast loading. Eur Phys J– Special Top 2016;225:265–82.

[29] Qu Y, Liu W, Gwarzo M, Zhang W, Zhai C, Kong X. Parametric study of anti-explosion performance of reinforced concrete T-shaped beam strengthened with steel plates. Constr Build Mater 2017;156:692–707.

[30] Yao S, Zhang D, Chen X, Lu F, Wang W. Experimental and numerical study on the dynamic response of RC slabs under blast loading. Eng Fail Anal 2016;66:120–9.

[31] Yang G, Wang G, Lu W, Yan P, Chen M. Damage assessment and mitigation measures of underwater tunnel subjected to blast loads. Tunn Undergr Space Technol 2019;94:103131. https://doi.org/10.1016/j.tust.2019.103131.

[32] Zhao X, Wang G, Lu W, Chen M, Yan P, Zhou C. Effects of close proximity underwater explosion on the nonlinear dynamic response of concrete gravity dams with orifices. Eng Fail Anal 2018;92:566–86.

[33] Pan Y, Ventura CE, Cheung MMS. Performance of highway bridges subjected to blast loads. Eng Struct 2017;151:788–801.

[34] Colombo M, Martinelli P, di Prisco M. On the blast resistance of high performance tunnel segments. Mater Struct 2016;49:117–31.

[35] Yoo D-Y, Banthia N. Mechanical and structural behaviors of ultra-high-performance fiber-reinforced concrete subjected to impact and blast. Constr Build Mater 2017;149:416–31.

[36] Li Y, Algassem O, Aoude H. Response of high-strength reinforced concrete beams under shock-tube induced blast loading. Constr Build Mater 2018;189:420–37.

[37] Pantelides CP, Garfield TT, Richins WD, Larson TK, Blakeley JE. Reinforced concrete and fiber reinforced concrete panels subjected to blast detonations and post-blast static tests. Eng Struct 2014;76:24–33.

[38] Bornstein H, Ryan S, Mouritz A. Physical mechanisms for near-field blast mitigation with fluid containers: Effect of container geometry. Int J Impact Eng 2016;96:61–77.

[39] Chaudhary RK, Mishra S, Chakraborty T, Matsagar V. Vulnerability analysis of tunnel linings under blast loading. Int J Protect Struct 2019;10(1):73–94.

[40] Gao Y, Zhou Y, Zhou J, Kong X, Zhang B, Liu S, et al. Blast responses of one-way sea-sand seawater concrete slabs reinforced with BFRP bars. Constr Build Mater 2020;232:117254.

[41] NS-EN 12390-3: Testing hardened concrete – Part 1: Shape, dimensions and other requirements for specimens and moulds. Standard Norge, 2012.

[42] Fagerholt E. Cited 22.08.2020. https://www.ntnu.edu/kt/ecorr.

[43] Kristoffersen M, Pettersen JE, Aune V, Børvik T. Experimental and numerical studies of the structural response of normal strength concrete slabs subjected to blast loading. Eng Struct 2018;174:242–55.

[44] Kristoffersen M, Langseth M, Børvik T. Combined three-point bending and axial tension of pressurised and unpressurised X65 offshore steel pipes – Experiments and simulations. Marine Struct 2018;61:560–77.

[45] C42/C42M: Standard test method for obtaining and testing drilled cores and sawed beams of concrete. American Society for Testing and Materials, 2019.

[46] NS-EN 12390-6: Testing hardened concrete – Part 6: Tensile splitting strength of test specimens. Standard Norge, 2009.

[47] Fourmeau M, Børvik T, Benallal A, Hopperstad OS. Anisotropic failure modes of high-strength aluminium alloy under various stress states. Int J Plast 2013;48: 34–53.

[48] Conrath EJ, Krauthammer T, Marchand KA, Mlakar PF. Structural Design for Physical Security: State of the Practice. American Society of Civil Engineers, 1999. ISBN 0-7844-0457-7.

[49] Kristoffersen M, Hauge KO, Børvik T. Blast loading of concrete pipes using C-4 charges. Proceedings 2018;2(8):428. https://doi.org/10.3390/ICEM18-05292.

[50] Krauthammer T. Modern protective structures. CRC Press, Taylor and Francis Group; 2008. ISBN 0-8247-2526-3.

[51] Nurick GN, Mahoi S, Langdon GS. The response of plates subjected to loading arising from the detonation of different shapes of plastic explosive. Int J Impact Eng 2016;89:102–13.

[52] Davids SA, Langdon GS, Nurick GN. The influence of charge geometry on the response of partially confined right circular stainless steel cylinders subjected to blast loading. Int J Impact Eng 2017.

[53] Irgens F. Continuum mechanics. Springer Verlag; 2008. ISBN 978-3-540-74297-5.

[54] Rushton N, Schleyer GK, Clayton AM, Thompson S. Internal explosive loading of steel pipes. Thin-Walled Struct 2008;46(7–9):870–7.

[55] Langdon GS, Ozinsky A, Yuen SCK. The response of partially confined right circular stainless steel cylinders to internal air-blast loading. Int J Impact Eng 2014;73: 1–14.

[56] Rigby SE, Tyas A, Bennett T, Warren JA, Fay S. Clearing effects on plates subjected to blast loads. Eng Comput Mech 2013;166:140–8.

[57] Wang W, Zhang D, Lu F, Wang S-C, Tang F. Experimental study and numerical simulation of the damage mode of a square reinforced concrete slab under close-in explosion. Eng Fail Anal 2013;27:41–51.

[58] IMPETUS AFEA SOLVER Command manual v. 5.0. IMPETUS AFEA AB, 02.10.2019. https://www.impetus-afea.com/support/manual/.

[59] Olovsson L, Limido J, Lacome J-L, Hanssen AG, Petit J. Modling fragmentation with new high order finite element technology and node splitting. Eur Phys J– Web Conf 2015;94.

[60] Thiagarajan G, Kadambi AV, Robert S, Johnson CF. Experimental and finite element analysis of double reinforced concrete slabs under blast loads. Int J Impact Eng 2015;75:162–73.

[61] Ruggieri P, Panontin TL, Dodds RH. Numerical modeling of ductile crack growth in 3-D using computational cell elements. Int J Fract 1996;82:67–95.

[62] Heggelund S, Brekken K, Ingier P, Christensen SO. Global response of a three-story building exposed to blast loading. Proceedings 2018;2(8):386. https://doi.org/10.3390/ICEM18-05211.

[63] Stander N, Roux W, Goel T, Eggleston T, Craig K. LS-OPT 5.0 User's Manual. Livermore Software Technology Corporation; 2012.

[64] Baltay P, Gjelsvik A. Coefficient of friction for steel on concrete at high normal stresses. J Mater Civ Eng 1990;2:46–9.

[65] Hill R. The mathematical theory of plasticity. Oxford University Press; 1950. ISBN 0-19-856162-8.

[66] Kristoffersen M, Casadei F, Børvik T, Langseth M, Hopperstad OS. Impact against empty and water-filled X65 steel pipes – Experiments and simulations. Int J Impact Eng 2014;71:73–88.

[67] Børvik T, Hopperstad OS, Berstad T, Langseth M. A computational model of viscoplasticity and ductile damage for impact and penetration. Eur J Mech A/ Solids 2001;20:685–712.

[68] Kristoffersen M, Hauge KO, Valsamos G, Børvik T. Blast loading of concrete pipes using spherical centrically placed C-4 charges. Eur Phys J– Web Conf 2018;183: 01057. https://doi.org/10.1051/epjconf/201818301057.

[69] Olovsson L, Hanssen AG, Børvik T, Langseth M. A particle-based approach to close-range blast loading. Eur J Mech A/Solids 2010;29(1):1–6.

[70] Børvik T, Olovsson L, Hanssen AG, Dharmasena KP, Hansson H, Wadley HNG. A discrete particle approach to simulate the combined effect of blast and sand impact loading of steel plates. J Mech Phys Solids 2011;59(5):940–58.

[71] Casadei F, Potapov S. Permanent fluid-structure interaction with non-conforming interfaces in fast transient dynamics. Comput Methods Appl Mech Eng 2004;193: 4157–94.

[72] Rigby SE, Akintaro OI, Fuller BJ, Tyas A, Curry RJ, Langdon GS, Pope DJ. Predicting the response of plates subjected to near-field explosions using an energy equivalent impulse. Int J Impact Eng 2019;128:24–36.

[73] Esteban B, Gebekken N. A comparison of numerical modelling strategies in contact detonation scenarios with concrete targets. Int J Comput Methods Exp Measur 2016;4(3):231–46. https://doi.org/10.2495/cmem-v4-n3-231-246.

[74] Chakraborty T, Larcher M, Gebekken N. Performance of tunnel lining materials under internal blast loading. Int J Protect Struct 2014;5(1):83–96.

[75] Shiravand MR, Parvanehro P. Numerical study on damage mechanism of post-tensioned concrete box bridges under close-in deck explosion. Eng Fail Anal 2017; 81:103–16.

[76] Codina R, Ambrosini D, de Borbón F. Alternatives to prevent the failure of RC members under close-in blast loadings. Eng Fail Anal 2016;60:96–106.

[77] Xu Z, Hao H, Li HN. Mesoscale modelling of fibre reinforced concrete material under compressive impact loading. Constr Build Mater 2012;26:274–88.

[78] Wang XF, Yang ZJ, Yates JR, Jivkov AP, Chang C. Monte Carlo simulations of mesoscale fracture modelling of concrete with random aggregates and pores. Constr Build Mater 2015;75:35–45.

[79] Rossi P, Wu X. Probabilistic model for material behaviour analysis and appraisement of concrete structures. Mag Concr Res 1992;44:271–80.